Charge density wave order in the kagome metal AV_3Sb_5 $(A=Cs, Rb, K)$

Shangfei Wu, Brenden R. Ortiz, Hengxin Tan, Stephen D. Wilson, Binghai Yan, Turan Birol, and Girsh Blumberg

Charge density wave order in kagome metal AV_3Sb_5 (A= Cs, Rb, K)

Shangfei Wu,[1, *] Brenden R. Ortiz,[2] Hengxin Tan,[3] Stephen D. Wilson,[2]
Binghai Yan,[3] Turan Birol,[4] and Girsh Blumberg[1, 5, †]

[1] *Department of Physics and Astronomy, Rutgers University, Piscataway, New Jersey 08854, USA*
[2] *Materials Department and California Nanosystems Institute,*
University of California Santa Barbara, Santa Barbara, California 93106, USA
[3] *Department of Condensed Matter Physics, Weizmann Institute of Science, Rehovot 7610001, Israel*
[4] *Department of Chemical Engineering and Materials Science, University of Minnesota, MN 55455, USA*
[5] *National Institute of Chemical Physics and Biophysics, 12618 Tallinn, Estonia*
(Dated: March 7, 2022)

We employ polarization-resolved electronic Raman spectroscopy and density functional theory to study the primary and secondary order parameters, as well as their interplay, in the charge density wave (CDW) state of the kagome metal AV_3Sb_5. Previous x-ray diffraction data at 15 K established that the CDW order in CsV_3Sb_5 comprises of a $2 \times 2 \times 4$ structure: one layer of inverse-star-of-David and three consecutive layers of star-of-David pattern. We analyze the lattice distortions based the $2 \times 2 \times 4$ structure at 15 K, and find that U_1 lattice distortion is the primary-like (leading) order parameter while M_1^+ and L_2^- distortions are secondary-like order parameters for Vanadium displacements. This conclusion is confirmed by the calculation of bare susceptibility $\chi_0'(q)$ that shows a broad peak at around $q_z = 0.25$ along the hexagonal Brillouin zone face central line (U-line). We also identify several phonon modes emerging in the CDW state, which are lattice vibration modes related to V and Sb atoms as well as alkali atoms. The detailed temperature evolution of these modes' frequencies, half-width-at-half-maximums, and integrated intensities support a phase diagram with two successive structural phase transitions in CsV_3Sb_5: the first one with a primary-like order parameter appearing at $T_S = 94$ K and the second isostructural one appearing at around $T^* = 70$ K. Furthermore, the T-dependence of the integrated intensity for these modes show two types of behavior below T_S: the low-energy modes show a plateau-like behavior below T^* while the high-energy modes monotonically increase below T_S. These two behaviors are captured by Landau free energy model incorporating the interplay between the primary-like and the secondary-like order parameters via trilinear coupling. Especially, the sign of the trilinear term that couples order parameters with different wave-vectors determines whether the primary-like and secondary-like order parameters cooperate or compete with each other, thus determining the shape of the T-dependence of the intensities of Bragg peak in x-ray data and the amplitude modes in Raman data below T_S. These results provide an accurate basis for studying the interplay between multiple CDW order parameters in kagome metal systems.

I. INTRODUCTION

Kagome lattice is a model system to study the electronic and magnetic properties [1, 2]. The corner shared triangle network of the kagome lattice enables three sublattice interference, which give rise to a variety of exotic physics, for example, flat bands, van Hove singularities, Dirac-dispersions in its electronic structure, frustrated magnetism, to name a few. Various electronic orders such as charge/spin density wave order, charge bond order, chiral flux order, nematic order, and superconductivity are under rigorous investigations [3–16].

Recently, a three-dimensional charge density wave (CDW) order, which coexists with superconductivity (SC) at low temperatures, was discovered in AV_3Sb_5 (A= Cs, Rb, K) kagome metals [Fig. 1(a)] [5, 15, 17–24]. Superconductivity emerges at $T_c = 1\sim3$ K, much lower than the CDW transition temperature ($T_S = 80\sim100$ K) [17–19]. Superconductivity competes with the CDW order

in AV_3Sb_5, as T_c increases when the CDW order is suppressed by hydrostatic pressure [24, 25], or by the hole doping [26–28], or by thickness reduction [28, 29]. Furthermore, the CDW state shows a large extrinsic anomalous Hall effect [30, 31] in the absence of magnetic ordering [32]. In the same CDW state, muon spin relaxation studies revealed a striking enhancement of the internal field just below T_S which persists into the SC state, suggesting time-reversal symmetry breaking [33, 34]. Thus, clarification of the symmetry, the nature, and the low temperature properties of the CDW order is pivotal for understanding the superconductivity in AV_3Sb_5 system.

The origin of the CDW order in AV_3Sb_5 remains under debate [5–11, 13, 20, 21, 35]. However, there is a consensus that CDW order leads to lattice distortions, which mostly consist of the displacements of Vanadium atoms in the kagome plane: The Inverse-Star-of-David (iSoD) type CDW [Fig. 1(c)] and the Star-of-David (SoD) type CDW [Fig. 1(d)] are obtained by the opposite sign displacements according to the same pattern [11, 21]. Both SoD and iSoD structure display an in-plane 2×2 modulation of the high-temperature structure [21], which is clearly demonstrated by scanning tunneling microscopy (STM)
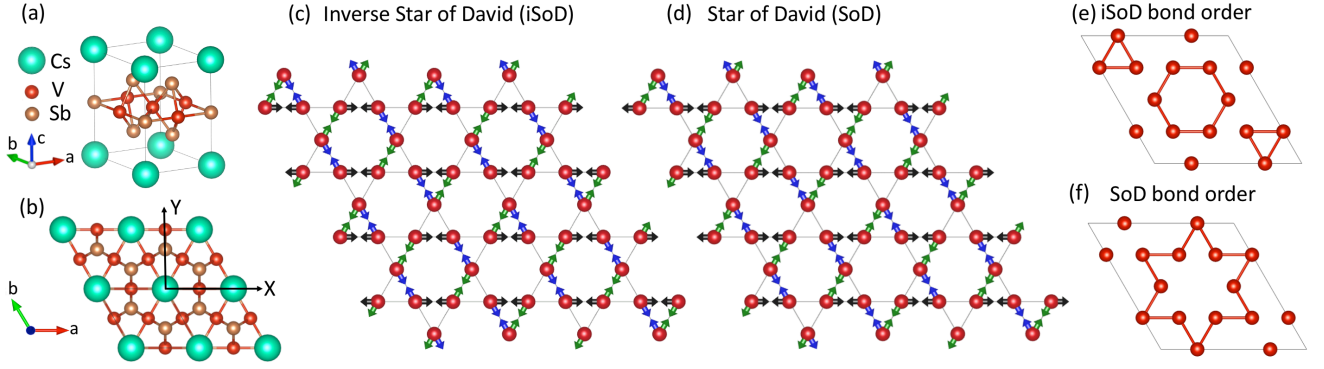
FIG. 1.   (a) Crystal structure of CsV_3Sb_5 in the high-temperature phase (space group: $P6/mmm$, No. 191, point group: D_{6h}). (b) Top view of the high-temperature crystal structure along the c axis and definitions of X and Y directions. (c) The inverse Star of David (iSoD) $2 \times 2 \times 1$ CDW phase. The black, blue, and green arrows represent the three V-V displacement directions. (d) The Star of David (SoD) $2 \times 2 \times 1$ CDW phase, which is obtained by merely reversing the direction of black arrows in (c). (e) The shorter V-V bond pattern for iSoD structure. (f) Same as (f) but for SoD structure.

measurements [15, 16, 20, 22]. Earlier x-ray diffraction measurements identified a three-dimensional $2 \times 2 \times 2$ CDW order in all AV_3Sb_5 compounds [18, 23]. However, more recent x-ray measurements reported a $2 \times 2 \times 4$ CDW order in CsV_3Sb_5 [36], highlighting nontrivial interlayer ordering along the c-axis direction. Furthermore, at an intermediate temperature T^* about 60–70 K, an additional uniaxial 1×4 charge modulation was reported by STM studies [15, 16, 22]. Ultrafast coherent phonon spectroscopy measurements [37–39], muon spin relaxation measurements [34], and transport studies [40, 41] all identified anomalies at around T^*, suggesting a secondary instability below T_S. Finally, density functional theory (DFT) phonon dispersion calculations found imaginary phonon frequencies at both $M(1/2, 0, 0)$ and $L(1/2, 0, 1/2)$ points [21], as well as at points along the U-line connecting the M and L momenta of the Brillouin zone for the high-temperature phase [11], indicating M_1^+, L_2^-, and U_1 lattice instabilities. These M_1^+, L_2^-, and U_1 lattice instabilities contribute to $2 \times 2 \times 1$, $2 \times 2 \times 2$, and $2 \times 2 \times 4$ CDW orderings, respectively. Which lattice instabilities give rise to the leading order parameter, and how it interplays with other lattice instabilities below the CDW transition in AV_3Sb_5 system, are not yet conclusively understood [11].

In this paper, we use polarization-resolved electronic Raman spectroscopy and DFT calculations to study the leading order parameter associated with the CDW transition in the kagome metal AV_3Sb_5. Prior x-ray diffraction data established that the CDW order in CsV_3Sb_5 has $2 \times 2 \times 4$ super-modulation structure with space group $P\bar{3}$: one layer of iSoD, alternating with three consecutive layers of SoD with zero-phase-shift between neighboring layers [36]. To a good approximation, the $2 \times 2 \times 4$ structure can be further refined to space group $P6/mmm$, which is the same space group for the high temperature undistorted kagome phase. By analyzing the Vanadium lattice distortions in the $2 \times 2 \times 4$ structure, we find that

U_1 lattice instability is primary-like while M_1^+ and L_2^- instabilities are secondary-like. This is also confirmed by the calculation of the bare static susceptibility $\chi_0'(q)$ that shows a broad peak at around $q_z = 0.25$ along the hexagonal Brillouin zone face central line (U-line).

These primary-like and secondary-like order parameters are revealed by Raman studies of the amplitude modes. We identify several new A_{1g} and E_{2g} phonon modes related to V and Sb atoms as well as alkali atoms displacements in the CDW state. Both the new A_{1g} and E_{2g} modes are the amplitude modes of the CDW order parameter. Especially, each A_{1g} new mode is a doublet that contains two modes close to each other. The detailed temperature evolution of the A_{1g} modes' frequency, half-width-at-half-maximum, and integrated intensity support two successive phase transitions in CsV_3Sb_5: the first one with a primary-like order parameter appearing at $T_S = 94$ K and the second isostructural one emerging at about $T^* = 70$ K. Moreover, we find two types of T-dependence of the integrated intensity for the new A_{1g} modes below T_S: The low-energy modes show a plateau-like behavior below T^* while the high-energy modes monotonically increase below T_S. These two behaviors are captured by Landau free energy model incorporating the interplay between the primary-like and the secondary-like order parameters via trilinear coupling.

The rest of this paper is organized as follows. In Sec. III, we present and discuss the theoretical and experimental results. Specifically, in Sec. III A, we first present an overview of the T-dependence of the Raman results. In Sec. III B, we introduce three lattice instabilities along the U-line, namely M_1^+, L_2^-, and U_1 instabilities. In Sec. III C, we examine the bare susceptibility $\chi_0'(q)$ along the U-line and establish an enhancement of $\chi_0'(q)$ at $q_z = 0.25$, which corresponds to the U_1 lattice instability. In Sec. III D 1, we discuss the crystal structure of CsV_3Sb_5 at 15 K and analyze the major lattice distortions in CsV_3Sb_5. In Sec. III D 2, we preform the

subduction analysis for the CDW phase. In Sec. III D 3, we construct a Landau free energy model to study the interplay between the primary-like and secondary-like order parameters. In Sec. III E 1, we show several Raman modes appearing in the CDW state and compare them in three AV_3Sb_5 systems. In Sec. III E 2, we discuss the temperature dependence of the main phonon modes in RR and RL scattering geometries in CsV_3Sb_5. In Sec. III E 3, we discuss the temperature dependence of the A_{1g} and E_{2g} amplitude modes in RR and RL scattering geometries in CsV_3Sb_5, respectively. Finally, in Sec. IV, we provide a summary of our observations and conclusions.

II. EXPERIMENT AND METHODS

A. Single crystal preparation and characterization

Single crystals of AV_3Sb_5 (A= K, Rb, Cs) were synthesized via the flux method described in Ref. [17–19], and the chemical compositions were determined by inductive coupled plasma analysis. These samples were characterized by electric transport and magnetic susceptibility measurements. The extracted structure phase transition (charge-density wave transition) temperatures T_S for AV_3Sb_5 (A= K, Rb, Cs) are $78\,K$, $103\,K$, and $94\,K$, respectively [17–19]. The sharpness of the Raman modes and the low residual spectra background [Fig. 2] indicate the high quality of the single crystals.

B. Raman scattering measurements

The as-grown samples were cleaved in the air to expose a fresh (001) crystallographic plane. The fresh cleaved surface was stable in the air, as we did cleave the crystals in N_2 atmosphere and found no noticeable changes in the Raman data. A strain-free area was examined by a Nomarski image. The cleaved crystals were positioned in a continuous helium flow optical cryostat. The Raman measurements were mainly performed using the Kr^+ laser line at $647.1\,nm$ ($1.92\,eV$) in a quasibackscattering geometry along the crystallographic c axis. The excitation laser beam was focused into a 50×100 μm^2 spot on the ab surface, with the incident power around $10\,mW$. The scattered light was collected and analyzed by a triple-stage Raman spectrometer, and recorded using a liquid nitrogen-cooled charge-coupled detector. Linear and circular polarizations were used in this study to decompose the Raman data into different irreducible representations. The instrumental resolution was maintained better than $1.5\,cm^{-1}$. All linewidth data presented were corrected for the instrumental resolution. The temperatures were corrected for laser heating, see Appendix A.

All spectra shown were corrected for the spectral response of the spectrometer and CCD to obtain the Raman intensity $I_{\mu v}$, which is related to the Raman response $\chi''(\omega, T)$: $I_{\mu v}(\omega, T) = [1 + n(\omega, T)]\chi''_{\mu\nu}(\omega, T)$.

TABLE I. The relationship between the scattering geometries and the symmetry channels. A_{1g}, A_{2g}, and E_{2g} are the irreducible representations of the D_{6h} point group.

Scattering Geometry	Symmetry Channel
XX	$A_{1g} + E_{2g}$
XY	$A_{2g} + E_{2g}$
RR	$A_{1g} + A_{2g}$
RL	$2E_{2g}$

Here μv denotes the polarization of $\mu(v)$ incident (scattered) photon, ω is energy, T is temperature, and $n(\omega, T)$ is the Bose factor.

The Raman spectra were recorded from the ab (001) surface for scattering geometries denoted as $\mu v = XX, XY, RR, RL$, which is short for $Z(\mu v)\bar{Z}$ in Portos notation, where X and Y denotes linear polarization parallel and perpendicular to the crystallographic axis, respectively; $R = X + iY$ and $L = X - iY$ denotes the right- and left-circular polarizations, respectively; The Z direction corresponds to the c axis perpendicular to the (001) plane, see Fig. 1(b). The polarization leakage from optical elements was removed in our data analysis, see Appendix B.

The relationship between the scattering geometries and the probed symmetry channels are summarized in Table I. The algebra used in this study to decompose the Raman data into three irreducible representations of the point group D_{6h} are summarized in Table II. More details are presented in Appendix C.

C. Density functional theory calculations

Density functional theory (DFT) calculations were performed within the Perdew-Burke-Ernzerhof-type generalized gradient approximation [42], which is implemented in the Vienna ab-initio Simulation Package (vasp) [43, 44]. The projected augmented wave potentials with 9 valence electrons for the A atom, 5 valence electrons for V, and 5 valence electrons for Sb were employed. The cutoff energy for the plane wave basis set was $300\,eV$. The zero damping DFT-D3 van der Waals correction was employed throughout the calculations. The phonon dispersion was calculated by using the finite displacement method as implemented in the phonopy code [45]. More details of phonon calculations are presented in Ref. [21].

TABLE II. The algebra used in this study to decompose the Raman data into three irreducible representations of the point group D_{6h}.

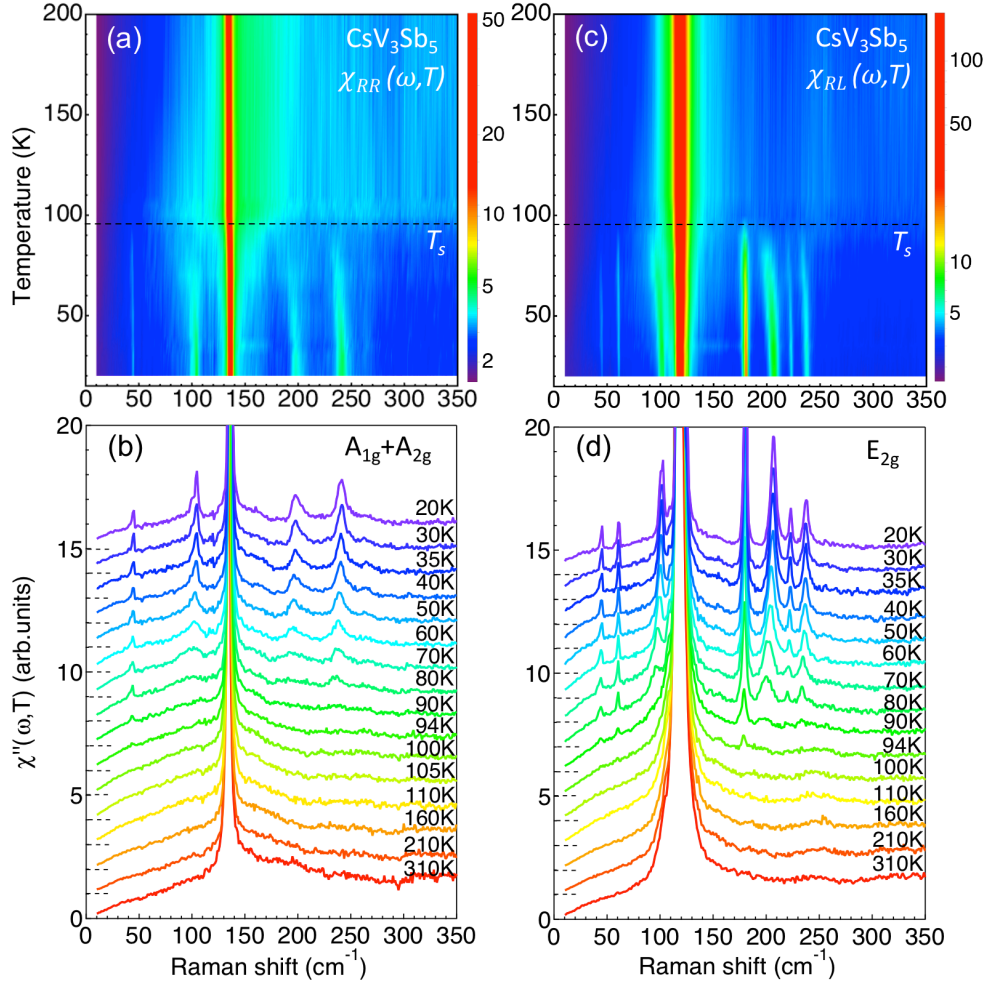| Symmetry Channel	Expression
A_{1g}	$\chi''^{D_{6h}}_{XX} - \chi''^{D_{6h}}_{RL}/2$
A_{2g}	$\chi''^{D_{6h}}_{XY} - \chi''^{D_{6h}}_{RL}/2$
E_{2g}	$\chi''^{D_{6h}}_{RL}/2$

FIG. 2. (a) The colorplot of the T-dependence of Raman spectra in RR [$A_{1g}+A_{2g}$] scattering geometry for CsV$_3$Sb$_5$. (b) The corresponding Raman spectra of (a). (c)-(d) Same as (a)-(b) but for RL [E_{2g}] scattering geometry. The dashed lines in (a) and (c) represent the structure phase transition temperature T_S. The dashed lines in (b) and (d) represent the level of zero for the vertically-shifted spectra.

The bare charge susceptibility were calculated via Eq. 1 and 2 where both intra- and inter-band contributions are considered [46]:

$$\chi'_0(\mathbf{q}) = \lim_{\omega \to 0} \chi'(\mathbf{q}, \omega) \sim \sum_{\mathbf{k}} \frac{f(\varepsilon_{\mathbf{k}}) - f(\varepsilon_{\mathbf{k+q}})}{\varepsilon_k - \varepsilon_{\mathbf{k+q}}} \qquad (1)$$

$$\lim_{\omega \to 0} \chi''(\mathbf{q}, \omega)/\omega \sim \sum_k \delta(\varepsilon_{\mathbf{k}} - \varepsilon_F) \delta(\varepsilon_{\mathbf{k+q}} - \varepsilon_F). \qquad (2)$$

$\chi'_0(\mathbf{q})$ and $\lim_{\omega \to 0} \chi''(\mathbf{q}, \omega)/\omega$ are the real and imaginary part of bare susceptibility, respectively. $f(\varepsilon)$ is the Fermi-Dirac distribution function. ε_k is the band dispersion, ε_F is the Fermi energy, and $\mathbf{q} = (q_x, q_y, q_z)$. The two parts for the high-temperatrue phase are calculated with a tight-binding Hamiltonian based on the maximally localized wannier functions [47]. The k-mesh for the Brillouin Zone integral is $150 \times 150 \times 80$. The temperature in

the Fermi-Dirac distribution is about $116\,\mathrm{K}$ ($\sim 10\,\mathrm{meV}$). For the imaginary part integral, the delta functions were replaced with the Lorentzian functions. The full width at half maximum for the Lorentzian function is about $10\,\mathrm{meV}$.

D. Symmetry analysis

The ISODISTORT tool [48], which is part of the ISOTROPY software suite, was used to analyze the lattice distortions in CsV$_3$Sb$_5$ shown in Table III. This procedure uses projection operators that decompose lattice distortions into separate irreducible representations (irreps) of the space group. The amplitudes of these irreducible representations can then be analyzed to identify the primary-like lattice distortions that have the largest amplitude below the structural phase transition, and
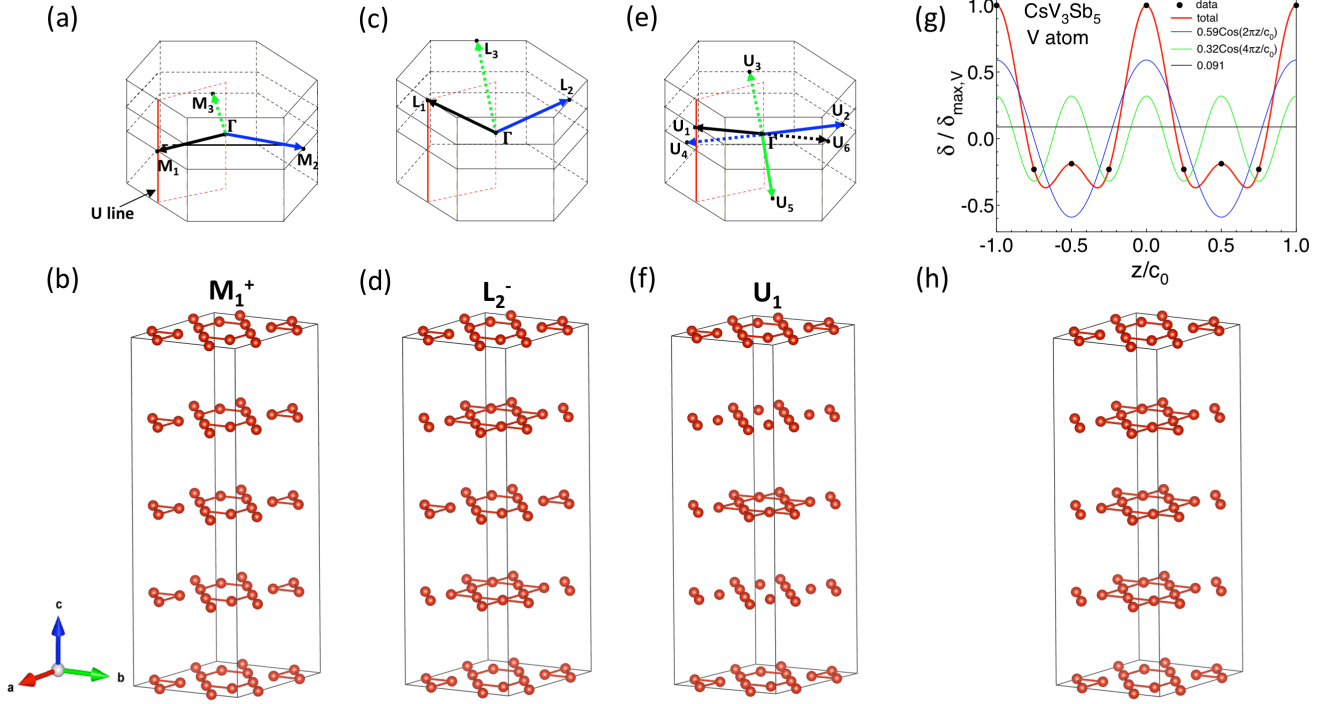
FIG. 3. The 3D hexagonal Brillouin zone (BZ) corresponds to the space group $P6/mmm$ with M, L, and U points highlighted, as well as the U-line connecting M and L shown in red. (a) The three vectors in the stars of M points, leading to $2 \times 2 \times 1$ CDW ordering shown as bond patterns in (b). (c) The three vectors in the stars of L points, contributing to $2 \times 2 \times 2$ CDW ordering shown as bond patterns in (d). (e) The six vectors in the stars of U points, which give rise to $2 \times 2 \times 4$ CDW ordering shown as bond patterns in (f). For these vectors shown in (a), (c), and (e), the solid arrows are pointing to the front faces while the dashed arrows are pointing to the back faces. (g) The normalized in-plane amplitude of V-displacements at $6j$ site $\delta/\delta_{max,V}$ in the kagome layer as a function of the normalized coordinate (z/c_0) for the $2 \times 2 \times 4$ structure of CsV_3Sb_5 at 15 K. c_0 is the c-axis lattice constant for the four-layer structure. The solid red, blue, and green lines represent the total fitted curve, the c_0-cosinusoidal modulation component, and the $c_0/2$-cosinusoidal modulation component, respectively. (h) Illustration of the $2 \times 2 \times 4$ structure for Vanadium lattice [36]. In (b), (d), (f), and (h), the Cs and Sb atoms are omitted for simplification.

the secondary-like distortions which have smaller amplitudes. We refrain from referring to these order parameters as 'primary' and 'secondary', and instead call them 'primary-like' and 'secondary-like', because there are trilinear terms present in the lattice Hamiltonian which can induce avalanche transitions. In such a phase transition, both order parameters set in together, but the transition disappears when the secondary-like order parameter is removed. The free energy expression in Eq. 6 was obtained following the same procedure in Ref. [11], and with the help of the INVARIANTS tool of the ISOTROPY software suite. The information for the irreducible representations of point groups and space groups follow the notations of Cracknell, Davies, Miller & Love [49], which is the same for the Bilbao Crystallographic Server [50, 51].

III. RESULTS AND DISCUSSIONS

A. Data overview

The high-temperature undistorted crystal of CsV_3Sb_5 has a hexagonal structure with space group $P6/mmm$ (#191) (point group: D_{6h}) above $T_S = 94$ K. Below T_S, the translational symmetries are broken and a three dimensional CDW order forms. In Fig. 2, we present an overview of the T-dependence of the Raman modes in both RR and RL scattering geometries for CsV_3Sb_5. In addition to one main phonon in RR scattering geometry and one main phonon in RL scattering geometry persisting across T_S upon cooling, several new phonons modes appear in both scattering geometries below T_S. The new modes in RL scattering geometry and the higher-energy modes in RR scattering geometry abruptly appear below T_S and gain intensity gradually upon cooling [Fig. 2(c)]. In contrast, the low-energy modes in RR scattering geometry first appear as relatively broad features which then sharpen upon cooling and gain intensity moder-
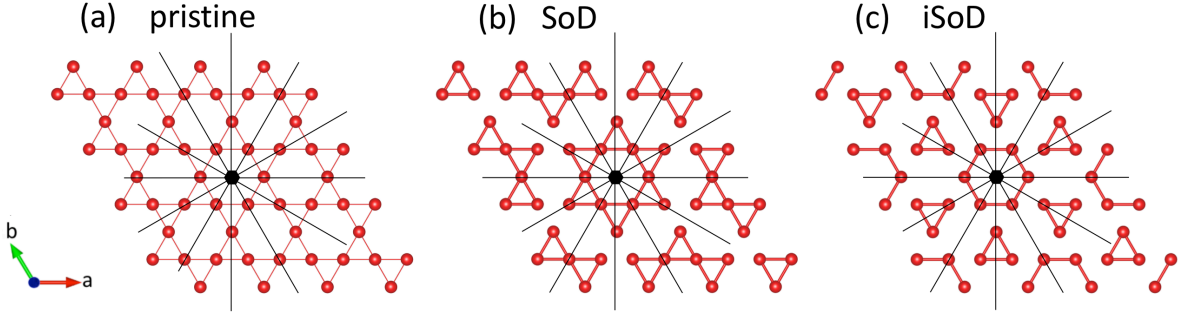
FIG. 4. Illustration of the D_{6h} point group symmetries of the high-temperature, SoD, and iSoD phase of CsV$_3$Sb$_5$. The black lines represent the mirror planes. The C_6 rotational symmetry is preserved in the above three phases. The Sb and Cs atoms are omitted for simplification.

ately [Fig. 2(a)]. In the following sections, we will discuss the nature of these modes, analyze the leading order parameters, the symmetry of the CDW ground state, and the origin of these two different behaviors for the new Raman modes below T_S.

B. Lattice instabilities at M, L, and U points

To begin with, we discuss the lattice instabilities in CsV$_3$Sb$_5$. Previous DFT calculations for this crystal structure find two unstable phonon modes at M and L points, as well as at the middle points of the U-line connecting the M and L momenta of the Brillouin zone [11, 21]. They transform as $M_1^+(a,a,a)$, $L_2^-(a,a,a)$, and $U_1(a,-a;a,-a;a,-a)$ irreducible representations of the space group $P6/mmm$. Formally, $M_1^+(a,a,a)$, $L_2^-(a,a,a)$, and $U_1(a,-a;a,-a;a,-a)$ are one-dimensional irreducible representations of the little group of the wave-vectors $M(1/2,0,0)$, $L(1/2,0,1/2)$ and $U(1/2,0,1/4)$, respectively. There are three vectors in the stars of both M and L points, as shown in Fig. 3(a) and (c), respectively. The star of U points has six vectors existing in three pairs. Within each pair, the two vectors are related to each other by inversion symmetry, as shown in Fig. 3(e). As a result, the M_1^+ and L_2^- space group representations are three-dimensional while the U_1 space group representation is six- dimensional.

For a single kagome layer, considering the M_1^+ instability, the equal-weight superposition of the three in-plane V-V displacements along the vectors shown in Fig. 3(a) lead to two distinct C_6-symmetric CDW orders. If all three components of V-V displacements have the same phase and equal amplitudes [Fig. 1(c)], the resulting shorter V-V bond pattern is the inverse Star-of-David (iSoD) bond-order shown in Fig. 1(e). On the other hand, if we shift the phase of one of the three V-V displacements by π while keeping the amplitudes the same [Fig. 1(d)], the resulting pattern is the Star-of-David (SoD) bond order shown in Fig. 1(f). Flipping the sign of two components of the order parameter, in other words, shifting the phase of two of the three V-V displacements by π, does not change the CDW pattern, but it shifts the CDW pattern by one unit cell, leading to a different domain of the same low-symmetry phase. While the translational symmetries are broken in the SoD and iSoD phases, they both possess the same set of mirror planes as the high-temperature structure, hence they have the same point group D_{6h}, as is illustrated in Fig. 4.

In real space, the only difference for M_1^+, L_2^-, and U_1 instabilities is the interlayer ordering for neighboring V kagome layers along the c-axis direction. For M_1^+ instability, all V atoms are displaced in-phase between the neighboring layers [Fig. 3(b)], corresponding a $2\times2\times1$ ordering. For L_2^- instability, all V displacements are out-of-phase between the nearest neighboring layers [Fig. 3(d)], leading to a $2 \times 2 \times 2$ ordering. For U_1 instability, all V displacements are out-of-phase between next-nearest-neighboring V layers [Fig. 3(f)], contributing to a $2\times2\times4$ ordering. Note that even when the L_2^- and U_1 order parameters set in (when the phase of displacements in neighboring kagome layers are not equal), it is possible to have mirror planes both normal to and in the plane of kagome layers. The equal-amplitude distortions of all three L_2^- or all six U_1 components give rise to the same $P6/mmm$ structures, but with enlarged $(2 \times 2 \times 2$ or $2 \times 2 \times 4)$ unit-cells. The realized CDW structure with $2 \times 2 \times 4$ supercell [Fig. 3(h)] can be a combination of the three lattice instabilities, namely, it is a superimposition of the three bond orders shown in Fig. 3(b), (d), and (f). Because the U_1 has lower symmetries than L_2^- or M_1^+, in other words, it breaks all the symmetries that L_2^- and M_1^+ break, these L_2^- and M_1^+ order parameters whose displacement patterns will be induced by U_1 can be regarded as secondary(-like) order parameters.

C. Bare susceptibility

In order to understand which lattice instabilities (M_1^+, L_2^-, and U_1) drive the CDW order in AV$_3$Sb$_5$, we examine the bare susceptibility $\chi_0(q_x, q_y, q_z)$.
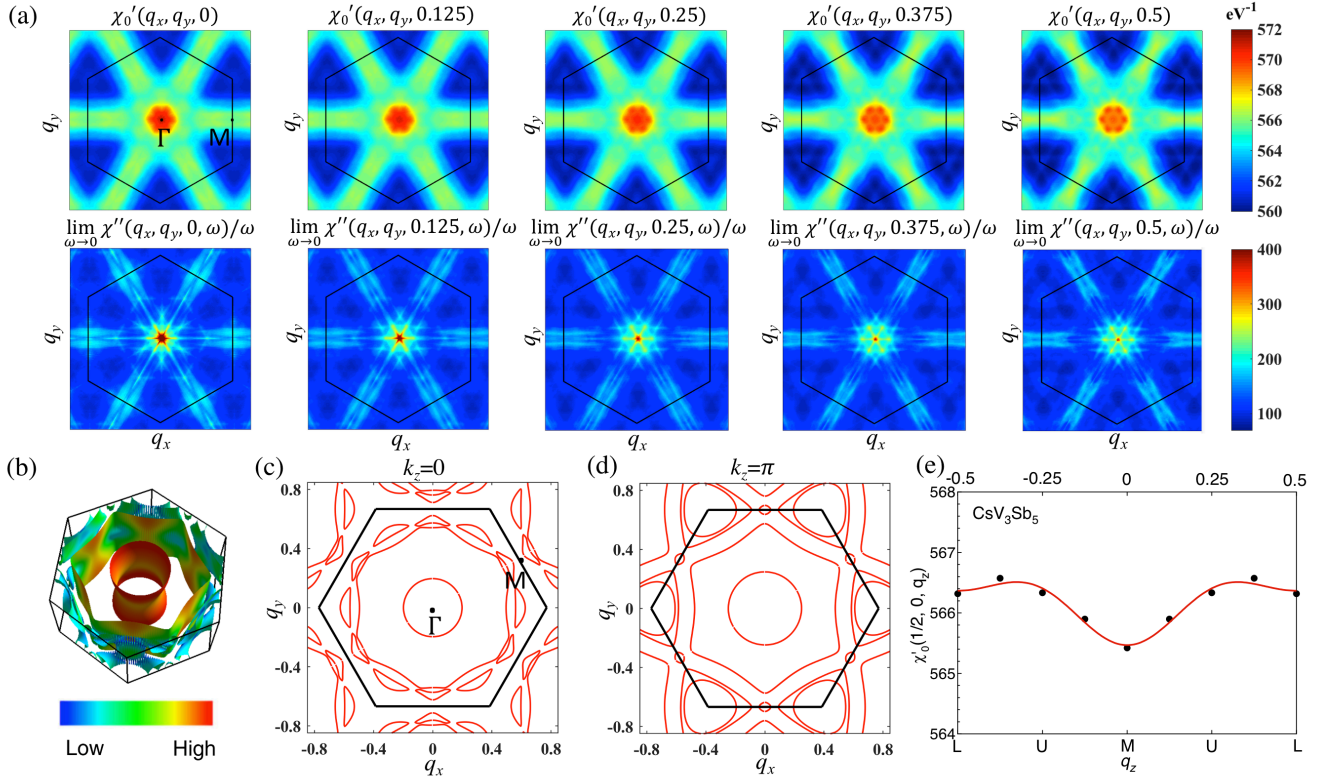
FIG. 5. (a) The bare susceptibility $\chi_0'(q_x, q_x, q_z)$ and $\lim_{\omega \to 0} \chi''(q_x, q_y, q_y, \omega)/\omega$ for CsV_3Sb_5 in the high-temperature phase for $q_z = 0$, 0.125, 0.25, 0.375 and 0.5, respectively. (b) Three dimensional Fermi surfaces for CsV_3Sb_5 adapted from Ref. [21]. (c) Two dimensional Fermi surface cut for CsV_3Sb_5 at $k_z = 0$. (d) Same as (c) but for $k_z = \pi$. (e) $\chi_0'(1/2, 0, q_z)$ along the $L - U - M - U - L$ line as a function of q_z. The solid red line is the guide line.

In Fig. 5(a), we show $\chi_0'(q_x, q_y, q_z)$ and $\lim_{\omega \to 0}[\chi''(q_x, q_y, q_y, \omega)/\omega]$ for CsV_3Sb_5 in the high-temperature phase with $q_z = 0, 0.125, 0.25, 0.375, 0.5$ at 116 K. The M_1^+, U_1, and L_2^- lattice instabilities locate in the $q_z = 0, 0.25, 0.5$ planes, respectively. For $q_z = 0$, $\chi_0'(q_x, q_y, 0)$ shows a broad enhancement along ΓM direction in the momentum space, indicating that Fermi surface nesting is marginal to drive the CDW transition. This result is also consistent with the Ref. [52]. Local minima are found at M points and ridges along ΓM direction exist around M point. Similar topography in $\chi_0'(q_x, q_y, q_z)$ is also found for nonzero $q_z = 0.125, 0.25, 0.375, 0.5$, as well as for $\lim_{\omega \to 0} \chi''(q_x, q_y, q_y, \omega)/\omega$. The ridges around ΓM lines originate from the 2D-like large hexagonal Fermi surface of V $3d$ band near Brillouin zone boundary [Fig. 5(b)]. Because the faces of the hexagon are relatively flat [Fig. 5(c)-(d)], the susceptibility along the ΓM direction parallel to the faces is large, resulting in the ridge along the ΓM direction. Due to the 2D-like Fermi surface [Fig. 5(b)], $\chi_0'(q_x, q_y, q_z)$ and $\lim_{\omega \to 0} \chi''(q_x, q_y, q_y, \omega)/\omega$ show little dependence of q_z [Fig. 5(a)].

In Fig. 5(e), we present $\chi_0'(1/2, 0, q_z)$ as a function of q_z along the U-line, namely $L - U - M - U - L$

line. $\chi_0'(1/2, 0, q_z)$ show a general enhancement along the whole U-line compared with BZ corner. This indicates the $L - U - M - U - L$ line is a line of lattice instabilities, which is the source for nontrivial interlayer orderings along the c-axis direction [18, 23, 36]. In particular, $\chi_0'(1/2, 0, q_z)$ shows a broad peak at around $|q_z| = 0.25$ along the U-line, which suggests that U_1 lattice instability is dominant compared with M_1^+ and L_2^- lattice instabilities.

Furthermore, due to the broad q−response, the calculated bare susceptibility $\chi_0'(q_x, q_y, q_z)$ does not indicate a single CDW ordering wavevector. The same is true also for the DFT phonon calculations [Appendix D]. Therefore, x-ray diffraction refinement data are required to settle the CDW ordering wavevector as well as the dominant lattice instability symmetry. These results will be presented in the next section.

We note that the true CDW instabilities can only be found from the full susceptibilities χ, not merely from the bare susceptibility χ_0. The full susceptibilities must account for both the electronic interactions and the interactions with the lattice. In addition, the local field effects might need to be considered in the calculations [52, 53].

D. x-ray diffraction analysis

1. Primary-like and secondary-like order parameters

For CsV_3Sb_5, the CDW order is established to be a $2 \times 2 \times 4$ structure below $T_S=94\,K$ [36]. It is refined within the space group $P\bar{3}$ assuming a minimal three-fold rotational symmetry and the inversion symmetry based on the x-ray diffraction data [36].

In Fig. 6, we show the refined $2 \times 2 \times 4$ structure for CsV_3Sb_5 at $15\,K$. It is composed of one layer of iSoD structure and three consecutive layers of SoD structures, with zero-phase-shift between neighboring layers. If we disregard the tiny distortions, $2 \times 2 \times 4$ structure can be further refined to higher-symmetry space group $P6/mmm$. The D_{6h} point group symmetries of the high-temperature phase are also preserved in this $2 \times 2 \times 4$ $P6/mmm$ structure, similar as the SoD and iSoD structure illustrated in Fig. 4.

To visualize the lattice distortion in the CDW phase, in Fig. 6, we show the displacement pattern for the $2 \times 2 \times 4$ $P6/mmm$ structure of CsV_3Sb_5 at $15\,K$. The most prominent distortions come from V atoms in the bottom kagome layer at $6l$ and $6j$ Wyckoff sites, which show iSoD-type distortions. These distortions are about 1% of the lattice constant, consistent with the 3~4 orders of magnitude weaker for the superlattice Bragg peak intensity compared with the fundamental lattice Bragg peak. The V atoms in the other three kagome layers at $6m$, $6k$, $12n$, and $12o$ Wyckoff sites show SoD-type distortions, which are about four times smaller than the iSoD layer. For Sb atoms, only the ones in bottom honeycomb layer at $4h$ and $12o$ Wyckoff sites show noticeable distortions, the rest ones in the other three layers hardly move. For Cs atoms, the distortions at $2e$ Wyckoff sites are tiny while the ones at $6i$ Wyckoff sites barely move in the CDW phase.

To quantitatively analyze these lattice distortions and figure out the leading order parameters, we use the ISODISTORT tool set [48] to list all the major distortions in Table III. From Table III, for V displacements, the $U_1(a, -a; a, -a; a, -a)$ distortion is the largest with an amplitude of 0.22 Å. This is the total displacement, summed over all V atoms in the $2 \times 2 \times 4$ $P6/mmm$

TABLE III. Analysis of major distortions in the refined $2 \times 2 \times 4$ $P6/mmm$ structure at $15\,K$ for CsV_3Sb_5 based on data in Ref. [36]. The units of the amplitude are Å.

Displacement	Instability	Amplitude
Sb	Γ_1^+	0.13
V	$M_1^+(a, a, a)$	0.05
V	$L_2^-(a, a, a)$	0.17
V	$U_1(a, -a; a, -a; a, -a)$	0.22
Cs	$L_2^-(a, a, a)$	0.03
Cs	$U_1(a, -a; a, -a; a, -a)$	-0.03

supercell. The $L_2^-(a, a, a)$ distortion is a bit smaller. The amplitude for $M_1^+(a, a, a)$ distortion is about 0.05 Å, much smaller than the $U_1(a, -a; a, -a; a, -a)$ distortion. Since the U_1 distortion is largest and it breaks all the in-plane and c-axis translational symmetries that are broken by L_2^- and M_1^+ order parameters, we refer to it as the primary-like order parameter while we refer to the $L_2^-(a, a, a)$ or $M_1^+(a, a, a)$ distortions as secondary-like order parameters [54].

Similar conclusions can be also reached by analyzing the normalized amplitude of V-displacements in the four kagome layers. In Fig. 3(g), we present the normalized in-plane amplitude of V-displacements ($\delta/\delta_{max,V}$) (at $6j$ sites in the first kagome layer, $12n$ sites in the second kagome layer, $6k$ sites in the third kagome layer) as function of z/c_0 coordinate (c_0 is the c-axis lattice constant for the 4-layer unit cell) at $15\,K$. The positive sign of $\delta/\delta_{max,V}$ represents the iSoD-type distortion while the negative sign represents the SoD-type distortion. We find that $\delta/\delta_{max,V}$ can be modeled by a sum of three components: a period of c_0 interlayer cosinusoidal modulation, a period of $c_0/2$ interlayer cosinusoidal modulation, and a constant. These three components correspond to U_1 [Fig. 3(f)], L_2^- [Fig. 3(d)], and M_1^+ [Fig. 3(b)] order parameters, respectively. The amplitude of c_0 interlayer modulation is about twice of $c_0/2$ interlayer modulation, consistent with previous distortion analysis for V displacements that U_1 order parameter is the dominant one that drives the $2 \times 2 \times 4$ CDW order while L_2^- order parameter is secondary-like. Similar conclusions can also be reached by analyzing V-displacements at $6l$ sites in the first kagome layer, $12o$ sites in the second kagome layer, $6m$ sites in the third kagome layer.

2. The symmetry of the order parameters

After establishing that U_1 instability is primary-like while L_2^- and M_1^+ instabilities are secondary-like for V displacements, in this section we focus on the symmetry of the order parameters in the CDW ground state [55].

We refer to the high-temperature structure's space group as $G_{1\times1\times1}$. Similarly, we refer to the space group of the $2 \times 2 \times 4$ supercell as $G_{2\times2\times4}$. Each symmetry of $G_{2\times2\times4}$ is a symmetry of $G_{1\times1\times1}$, but the opposite is not true, because the translation by a primitive lattice vector is no longer a symmetry in the $2 \times 2 \times 4$ structure. When the symmetry is reduced from $G_{1\times1\times1}$ to $G_{2\times2\times4}$ due to the reduced translational symmetry, the irreducible representations of $G_{1\times1\times1}$ may become reducible representations of $G_{2\times2\times4}$. The originally unstable M_1^+, L_2^- and U_1 modes of the high-temperature structure get folded back to the center of the Brillouin zone for the low-temperature structure. The list of the irreducible representations subducted from the irreducible representations of $G_{1\times1\times1}$ for $G_{2\times2\times4}$ are:

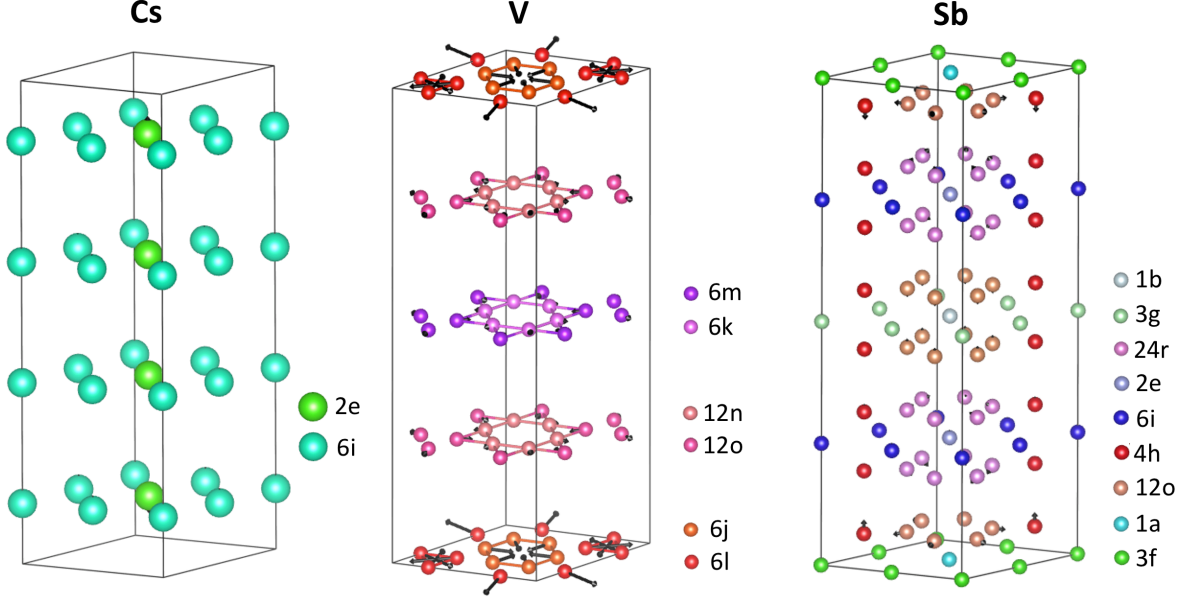$$M_1^+ {\downarrow} G_{2\times2\times4} = \Gamma_1^+ + \Gamma_5^+ \qquad (3)$$

FIG. 6. Wyckoff-site dependent displacement pattern for CsV_3Sb_5 in the $2 \times 2 \times 4$ CDW phase at 15 K [36]. The Wyckoff sites are indexed according to the space group $P6/mmm$ based on the unit cell of the $2 \times 2 \times 4$ CDW phase. The arrows represent the direction of displacement for specific atoms at 15 K. The length of arrows for different atoms are scaled for visualization propose.

$$L_2^- \downarrow G_{2 \times 2 \times 4} = \Gamma_1^+ + \Gamma_5^+ \tag{4}$$

$$U_1 \downarrow G_{2 \times 2 \times 4} = \Gamma_1^+ + \Gamma_5^+ + \Gamma_2^- + \Gamma_5^- \tag{5}$$

Eq. 3, Eq. 4, and Eq. 5 show the symmetry-allowed order parameters with specific irreducible representation symmetries that can emerge in the ordered state due to the corresponding M_1^+, L_2^-, and U_1 instabilities. For example, U_1 instability leads to 4 potential order parameters in the $2 \times 2 \times 4$ ground state: Γ_1^+ (which corresponds to the point group irreducible representation A_{1g}, Raman active, z^2 or $x^2 + y^2$), Γ_5^+ (which corresponds to E_{2g}, Raman active, $x^2 - y^2$ or xy), Γ_2^- (which corresponds to A_{2u}, infrared active, z), and Γ_5^- (which corresponds to E_{2u}).

The Γ_1^+ (A_{1g}) is the fully symmetric irreducible representation and Γ_5^+ (E_{2g}) is the 2D irreducible representations. Both representations are Raman active [56]. According to Eq. 5, only a single unstable phonon in the high-temperature structure freeze below the phase transition temperature, and becomes the order parameter with a nonzero expectation value in the ground state. This realizes the global minimum of the free energy, and transforms as $\Gamma_1^+(A_{1g})$ in the low-temperature structure.

The other unstable modes in Eq. 5 can be thought of as the "failed order parameters" that would appear as low energy oscillations of the order parameter. The excitations into the "failed order parameters" could be accessed spectroscopically by exciting the amplitude modes of the "failed order parameters".

Γ_5^+ (E_{2g}), one of the "failed order parameters", breaks the three-fold rotational symmetry. This "nematic"-like C_3-symmetry broken phase could be stabilized on the surface, which is predicted for a real CDW ordering with $k_z \neq 0$ due to the three dimensional coupling [8]. It might explain the rotational symmetry breaking due to uniaxial charge modulation observed by STM [15, 16, 22], two-fold c-axis magnetoresistance below T_S [40, 41], the enhanced $m_{11} - m_{12}$ elasto-resistance coefficient above T_S [57], as well as the two-fold-like amplitude of coherent phonon mode observed in the pump-probe Kerr rotation measurement [39].

3. Interplay between the primary-like and secondary-like order parameters

In this section, we use a phenomenological model at the level of Landau free energy expansion to study the interplay between the primary-like and secondary-like order parameters for V displacements in the ground state with Γ_1^+ (A_{1g}) symmetry.

Since the amplitude of the secondary-like M_1^+ distortion is significantly smaller than the L_2^- and U_1 distortions of V displacements [Table III], we neglect M_1^+ distortion. For the specific domain and order parameter directions of L_2^- and U_1, the free energy is

$$\mathcal{F}(T) = \alpha_u(T)u^2 + \alpha_l(T)l^2 + \gamma u^2 l + \beta u^2 l^2 + \lambda_u u^4 + \lambda_l l^4, \tag{6}$$

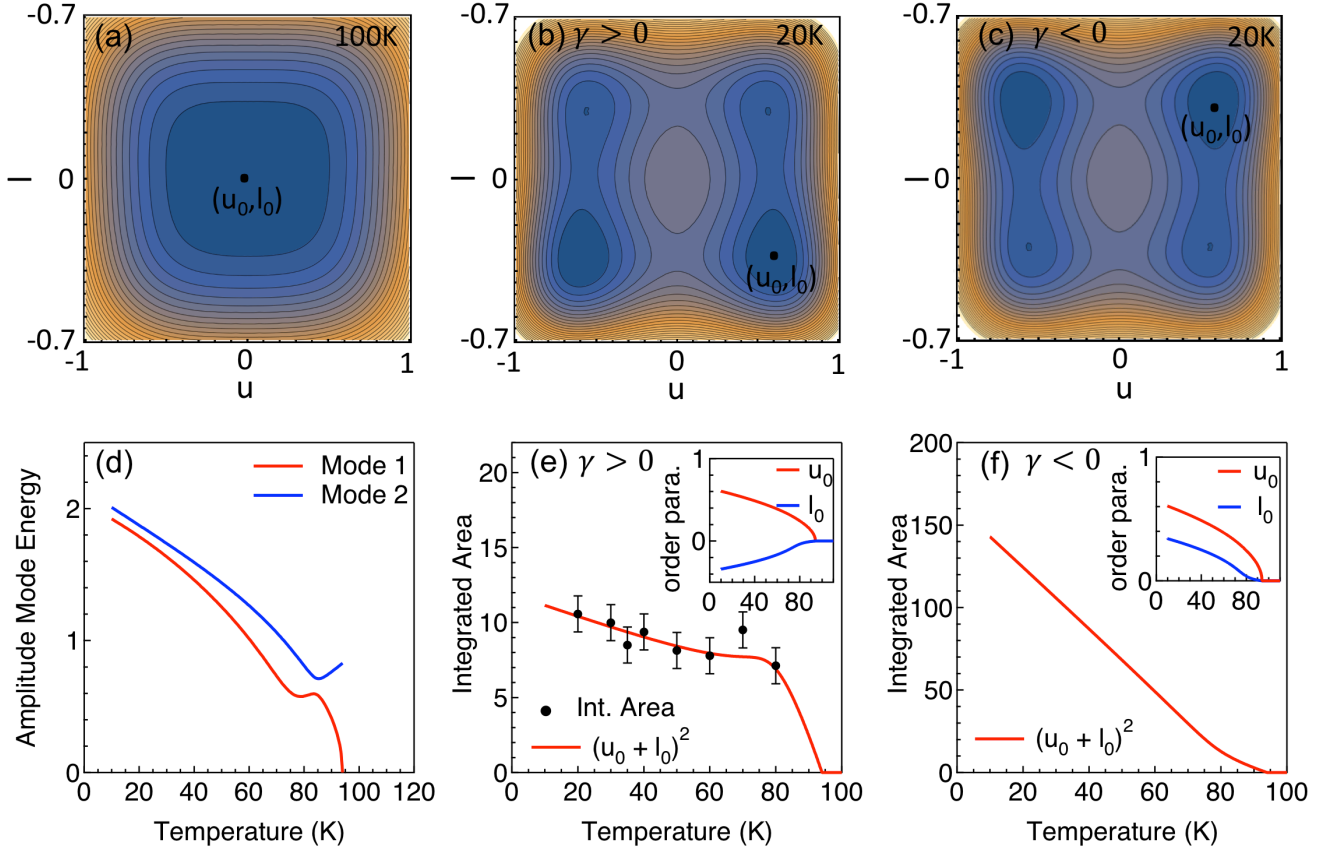where u and l represent the U_1 and L_2^- order parameters,

FIG. 7. Illustration of the Landau free energy model Eq. 6. The parameters used in the model are $\alpha_{u0} = -1$, $\alpha_{l0} = -1$, $\gamma = 0.2$, $\beta = 0.1$, $\lambda_u = 1.3$, $\lambda_l = 4$, $T_S = 94$, and $T^* = 70$. (a) The free energy at 100 K. (b) The free energy at 20 K. (c) The free energy at 20 K in the case of $\gamma = -0.2$ while the other parameters remain unchanged. In (a)-(c), the global minima is represented by a black dot at (u_0, l_0). (d) T-dependence of the A_{1g} amplitude mode frequencies for mode 1 and mode 2. (e) T-dependence of $(u_0 + l_0)^2$. The black solid circles represent the T-dependence of the integrated intensity for the A_{1g} 105 cm^{-1} mode in CsV$_3$Sb$_5$. The inset of (e) shows the T-dependence of $u_0(T)$ and $l_0(T)$ order parameters. (f) T-dependence of $(u_0 + l_0)^2$ in the case of $\gamma = -0.2$ while the other parameters remain unchanged. The inset of (f) shows the T-dependence of $u_0(T)$ and $l_0(T)$ order parameters.

respectively. α_u, α_l, λ_u, and λ_l are coefficients while γ and β are coupling constants between u and l. This form of free energy is found by considering every polynomial, up to 4th-order, of the order parameters that remain invariant under each symmetry operation of the high-temperature space group. The $\gamma u^2 l$ term is the trilinear term while the $\beta u^2 l^2$ terms is the biquadratic coupling term. They involve coupling between different order parameters [11].

According to DFT phonon calculations which are performed at zero temperature [11, 21], both the U_1 and L_2^- modes are unstable. Therefore, both α_u and α_l are negative at zero temperature; however at high temperature they must both be positive so that the non-symmetry-broken structure is retained. There is no symmetry argument that sets the temperature at which these parameters cross zero, so one can set $\alpha_u(T) = \alpha_{u0}(T - T_S)$ and $\alpha_l(T) = \alpha_{l0}(T - T^*)$ without loss of generality. Doing this, and minimizing the free energy Eq. 6 with respect

to u and l, we can obtain the solution of $u_0(T)$ and $l_0(T)$, as well as the corresponding free energy $\mathcal{F}(T)$.

As shown in Fig. 7(a), well above T_S the free energy has a single minimum at $(0,0)$. Reducing the temperature near T_S, nonzero order parameters u_0 and l_0 develop. The free energy develops two minima in the parameter space. Depending the sign of the parameter γ, the global minimum appears in a different part of the parameter space. Suppose a case that $\gamma > 0$ and the global minimum appears where $u_0 > 0$ and $l_0 < 0$ [Fig. 7(b)]. If we reverse the sign of γ, the global minimum locates where $u_0 > 0$ and $l_0 > 0$ [Fig. 7(c)]. This conclusion also holds when $u < 0$ such as in a domain structure, because $\mathcal{F}(T)$ is even with respect to u. In the insets of Fig. 7(e) and (f), we show the solution $u_0(T)$ and $l_0(T)$ corresponding to the global minimum in Fig. 7(b) and (c), respectively. In both cases, the transition is first order and both order-parameters have a discontinuity at the transition temperature, but the primary-like order

parameter $u_0(T)$ develops more sharply below T_S while the secondary-like order parameter $l_0(T)$ develops gradually below T_S.

The T-dependence of the square of the order parameters $(u_0 + l_0)^2$ can distinguish how the primary-like and secondary-like order parameter interplay with each other. In Fig. 7(e), we show the T-dependence of $(u_0+l_0)^2$ in the case of $\gamma > 0$ where u_0 and l_0 have different signs. In this case, u_0 and l_0 interplay with each other destructively. As a consequence, $(u_0 + l_0)^2$ shows a plateau-like behavior below T^*. In Fig. 7(f), we show the T-dependence of the $(u_0 + l_0)^2$ in the case of $\gamma < 0$ where u_0 and l_0 have the same signs. In this case, u_0 and l_0 interplay with each other constructively. Thus, $(u_0 + l_0)^2$ increases monotonically below T_S. These two behaviors can be tested by the temperature-dependence of the amplitude modes' integrated intensities, which will be discussed in Section III E 3.

Moreover, the T-dependence of $(u_0 + l_0)^2$ also implies the properties of the second phase transition at T^*. For V displacements, the first transition at T_S is driven by the primary-like U_1 order parameter, it breaks both the in-plane and c-axis translational symmetries at T_S. The secondary-like order parameter L_2^- appears by coupling to the primary-like order parameter below T_S. The second transition involves mostly a change in the secondary-like order parameter's amplitude at T^*. This second transition is isostructural, and results in no change in the symmetry of the crystal. As a consequence, this second transition at T^* is necessarily first order according to group theory.

Finally, we discuss the T-dependence of the A_{1g} amplitude modes frequencies. We expand the free energy $\mathcal{F}(T)$ at the minimum position (u_0, l_0). Taking the second derivative of $\mathcal{F}(T)$ with respect to u and l, and solving the eigenvalue of the following equation:

$$\begin{vmatrix} \partial^2\mathcal{F}/\partial u^2 - m\omega^2 & \partial^2\mathcal{F}/\partial u\partial l \\ \partial^2\mathcal{F}/\partial l\partial u & \partial^2\mathcal{F}/\partial l^2 - m\omega^2 \end{vmatrix}_{u=u_0(T),l=l_0(T)} = 0, \tag{7}$$

we obtain the T-dependences of two normal A_{1g} amplitude mode frequencies ω around the free energy minima at (u_0, l_0) [58]. We note that there are two solutions of A_{1g} amplitude mode frequencies based on Eq. 7, suggesting that each A_{1g} amplitude mode is doublet that contains two modes close to each other in this system.

In Fig. 7(d), we show an example of the T-dependence of the two amplitudes modes frequencies below T_S. Mode 1 increases gradually from zero below T_S. Mode 2 first decreases, showing an upturn, and then increases gradually. Both Mode 1 and Mode 2 show a clear anomaly at around 80 K, which is close to T^* that is set to be 70 K in the free energy model. The anomalies at around T^* are due to the interplay between the primary-like and secondary-like order parameters, because the frequencies of Mode 1 and Mode 2 are expected to show mean-field like behavior (square root of $T_S - T$) in the case of $\gamma = 0$ and $\beta = 0$.

E. Raman results

In the previous sections, we have established the primary and secondary-like order parameters for V displacements, and the interplay between them in the free energy model. In this section, we illustrate how they are reflected in the Raman data.

1. Phonon modes

From the group theoretical considerations of the high-temperature structure, Γ point phonon modes of the hexagonal AV$_3$Sb$_5$ are expressed as $\Gamma_{\text{total}} = A_{1g} + 4A_{2u} + B_{1g} + B_{1u} + 2B_{2u} + 2E_{2u} + E_{2g} + 5E_{1u} + E_{1g}$. Raman active modes are $\Gamma_{\text{Raman}} = A_{1g} + E_{2g} + E_{1g}$. Note that A_{1g} and E_{2g} phonons can be measured from the ab-plane measurement while the E_{1g} phonon can only be accessed from the ac surface.

In Fig. 8(a)-(d), we compare the phonon modes of CsV$_3$Sb$_5$ above and below T_S (94 K) measured in four different scattering geometries. Above T_S, as shown in Fig. 8(a), the sharp phonon mode at around $119\,\text{cm}^{-1}$ detected in XX, XY, and RL scattering geometries corresponds to the E_{2g} phonon, which is the in-plane lattice vibration of the Sb atoms in the honeycomb net. The other sharp phonon at $137\,\text{cm}^{-1}$ detected in XX and RR scattering geometries corresponds to the A_{1g} phonon. It is the c-axis lattice vibration of the Sb atoms in the honeycomb net. As we show the symmetry decompositions in Fig. 8(b), the E_{2g} and A_{1g} phonon modes are clearly separated into the E_{2g} and A_{1g} channels, respectively.

Below T_S (94 K), new phonon modes are expected to appear in the CDW state [59]. While there are $26A_{1g} + 33E_{2g} + 35E_{1g}$ Raman active modes in the $2\times2\times4$ structure due to BZ folding [Appendix E], only those modes modulating the ionic deviation from the high temperature structure [Fig. 6] with a large amplitude can gain noticeable Raman intensity, thus can be detected in the Raman spectra [55, 60, 61]. These modes are the amplitudes modes of the CDW order parameter. The new A_{1g} modes are the amplitudes modes of the CDW ground state while the new E_{2g} modes are the amplitudes modes of the 'failed order parameters' [Section III D 2]. Specifically, in the case of dual order parameters, each new A_{1g} mode is a doublet at low temperatures [Section III D 3].

In Fig. 2 and Fig. 8(c), we show several new phonon modes appearing in all four scattering geometries below T_S. The intensities of these new phonons mode are generally two order of magnitude weaker than the main phonon peak at $119\,\text{cm}^{-1}$ and $137\,\text{cm}^{-1}$, consistent with the weak superlattice Bragg peaks observed in the x-ray scattering measurements [23, 36]. The symmetry of these new phonon modes can be clearly distinguished by decompositions according to the point group D_{6h} shown in Fig. 8(d). This indicates that the three-fold rotational symmetry remains intact in the CDW phase [Ap-
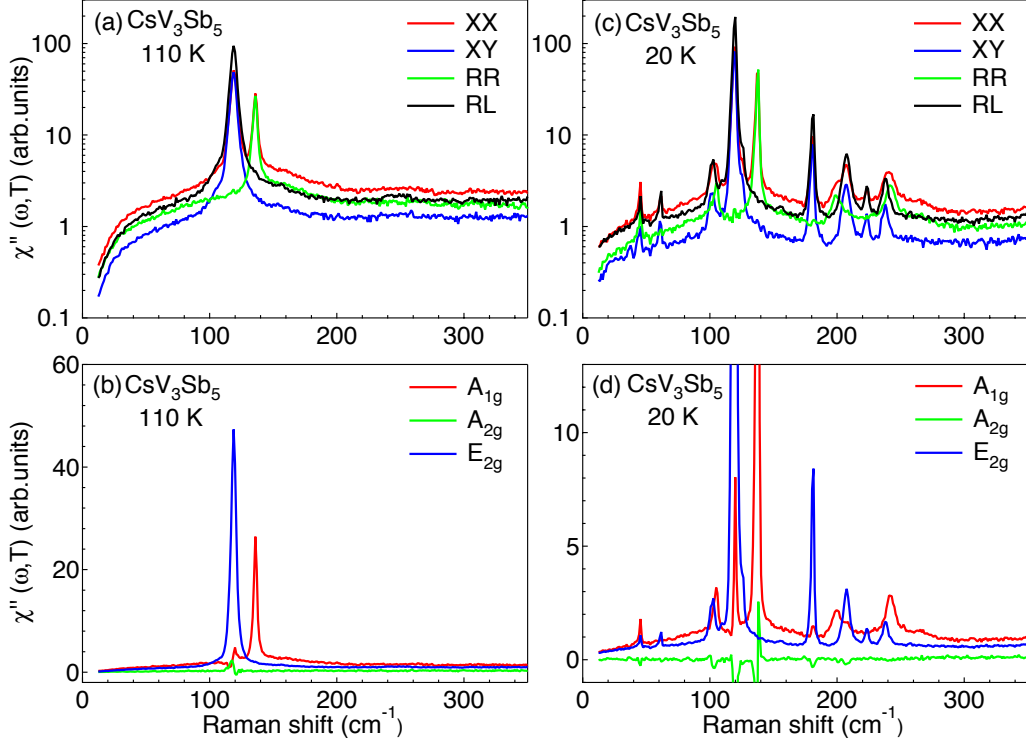
FIG. 8. Symmetry-resolved spectra of CsV_3Sb_5 above and below T_S. (a) Raman spectra of CsV_3Sb_5 on a cleaved ab surface for the XX, XY, RR, and RL scattering geometries at 110 K. (b) Symmetry decompositions into separate irreducible representations according to the point group D_{6h} using the algebra shown in Table II. (c) and (d) Same as (a)-(b) but at 20 K.

pendix C].

Specifically, 3 additional doublet modes are detected in the A_{1g} channel, and 7 additional modes are observed in the E_{2g} channel below T_S. These new phonon peak positions are summarized in Table IV. From Table IV, we find that the experimentally observed phonon frequencies for CsV_3Sb_5 at 20 K agree with the DFT phonon calculations based on the $2 \times 2 \times 1$ iSoD structure, suggesting the iSoD-type distortion is dominant in the CDW ground state. This is consistent with the major iSoD-type displacement patterns in the x-ray results [Fig. 6].

It deserves to remark on the charge density gaps which are about $2\Delta \approx 40$ meV determined by STM [20], ARPES [35, 62, 63], and ultrafast measurements [38]. The CDW gap opening signatures, namely the suppression of the low-energy spectra weight and the enhancement of the spectra weight close to $2\Delta \approx 40$ meV, are not observed in the Raman response both in the A_{1g} and E_{2g} channels. The absence of CDW gap opening signatures may be due to the multiband effects in AV_3Sb_5 system.

We note that if the inversion symmetry does not hold, the infrared-active A_{2u} and E_{1u} modes will become Raman-active. However, no such modes are observed [Table IV]. Thus, the inversion symmetry remains intact in the CDW phase, consistent with the second harmonic generation measurements [34, 36] and the x-ray

diffraction results [36].

After establishing the new phonon modes in the CDW phase of CsV_3Sb_5, it is instructive to take a closer look at their sibling compounds RbV_3Sb_5 and KV_3Sb_5. In Fig. 9(a) and (b), we compare the Raman response in RR and RL scattering geometries for the three compounds. In general, the spectral features for all three compounds are similar. They show similar number of new phonon modes at similar positions at 20 K. The summary of the new phonon modes for the three compounds at 20 K are presented in Table IV.

According to the group theoretical analysis, for the $2 \times 2 \times 1$ SoD or iSoD phase, all the Raman-active phonon modes are related to the V atoms in the kagome net and Sb atoms in the honeycomb net. The lattice vibration for the alkali atoms (Cs, K, Rb) are forbidden. However, they become Raman-active in the $2 \times 2 \times 4$ structure [Appendix E]. Based on Table IV, all the phonon frequencies decrease when switching from Cs to K, except for the low-energy modes showing both A_{1g} and E_{2g} symmetries, e.g. 45 cm^{-1} mode in CsV_3Sb_5. The distinct behavior for this phonon with A_{1g} and E_{2g} symmetry indicates it does not come from kagome net nor from the honeycomb net. Based on the fact that (1) Cs is the heaviest atom in CsV_3Sb_5, it should have the lowest vibration frequency; (2) The atomic mass deceases when switching from Cs to
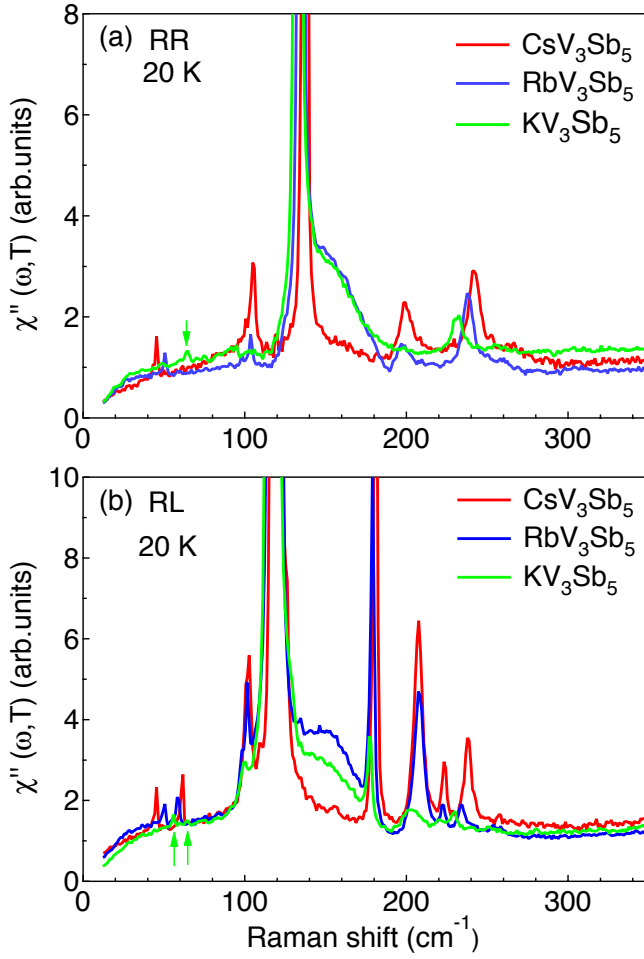
FIG. 9. (a) Comparison of the Raman spectra taken in RR $[A_{1g}+A_{2g}]$ scattering geometry for the three compounds CsV_3Sb_5, RbV_3Sb_5, KV_3Sb_5. (b) Same as (e) but in RL $[E_{2g}]$ scattering geometry. The green arrows in (e) and (f) locate the weak low-energy phonons for KV_3Sb_5.

K in AV_3Sb_5, the vibration frequency are expected to increase, we conclude that the low-energy phonon modes at $45\,cm^{-1}$ in CsV_3Sb_5, $51\,cm^{-1}$ in RbV_3Sb_5, and $64\,cm^{-1}$ in KV_3Sb_5 must be the alkali-atom-related lattice vibration modes [Appendix E]. Furthermore, these modes appear for all four scattering geometries, thus they do not obey the D_{6h} selection rules [Table I, II], suggesting they are not bulk phonons. Moreover, the amplitude of the mode at $45\,cm^{-1}$ in CsV_3Sb_5 show two-fold rotational symmetry in the pump-probe Kerr rotation measurement at $20\,K$ [39], indicating a C_3-symmetry broken phase. This "nematic"-like C_3-symmetry broken phase would be characterized by the "failed order parameter" with Γ_5^+ (E_{2g}) symmetry that is stabilized on the surface [Section III D 2]. Indeed, the alkali surface reconstruction, namely the half alkali surface, is most commonly observed in STM experiments [16].

However, we notice several quantitative differences for

TABLE IV. The phonon frequencies calculated by DFT for the $2 \times 2 \times 1$ SoD and iSoD structure for CsV_3Sb_5 and the experimentally observed phonon frequencies at Brillouin zone center for the three compounds AV_3Sb_5 (A=Cs, Rb, K) at $20\,K$. All the units are in cm^{-1}.

Sym.	CsV_3Sb_5 SoD (DFT)	CsV_3Sb_5 iSoD (DFT)	CsV_3Sb_5 (Exp)	RbV_3Sb_5 (Exp)	KV_3Sb_5 (Exp)
	227	242	241,262	238,260	231,254
	200	203	197,202	196,201	
A_{1g}	143	142			
	124	132	137	136	133
	93	108	99,105	98,104	92,95
			45	51	64
	247	234	238	234	230
	219	221	223	223	220
	172	212	208	208	202
	169	175	181	179	177
E_{2g}	130	129			
	120	125	119	119	117
	55	99	102	101	100
	50	58	61	59	56
			45	51	64

the three compounds AV_3Sb_5 (A=Cs, Rb, K). First, the intensity of the new phonon modes are the strongest in CsV_3Sb_5 among the three compounds; it becomes weaker in RbV_3Sb_5 and becomes much weaker in KV_3Sb_5. We note that the amplitude of specific jump at T_S for KV_3Sb_5 is also the smallest among the three systems [17–19, 64]. Second, the scattering rate for the main phonon modes is the smallest for CsV_3Sb_5 and the largest for KV_3Sb_5 [Table V]. This might explain why the new phonon intensity in KV_3Sb_5 is weaker, as there might be more disorders or stacking faults in KV_3Sb_5 than the other two systems. Third, there is a broad peak centered at around $150\,cm^{-1}$ for RbV_3Sb_5 and KV_3Sb_5 in both RR and RL scattering geometries [23, 65], but not noticeable for CsV_3Sb_5.

2. Temperature dependence of main modes

After establishing the phonon modes in the three AV_3Sb_5 systems, we switch to study the T-dependence

TABLE V. Comparison of phonon scattering rate for the main A_{1g} and E_{2g} phonons at $20\,K$ for the three compounds AV_3Sb_5 (A=Cs, Rb, K). The phonon scattering rate is obtained as the inverse of the HWHM. All the HWHM data have been corrected for the instrumental resolution. The unit of scattering rate is in GHz.

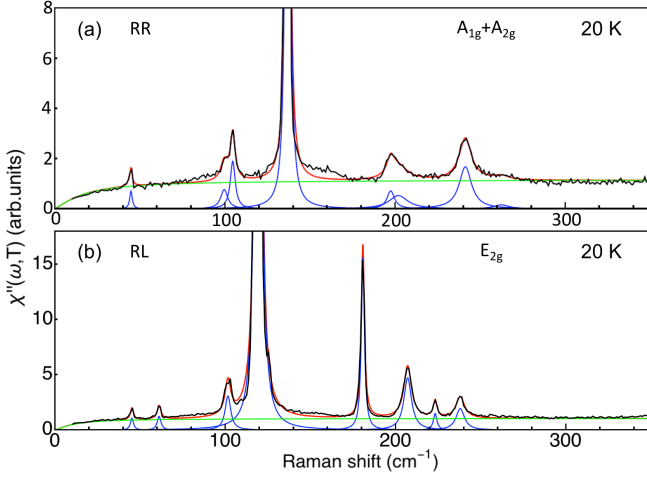| sample	A_{1g}	E_{2g}
CsV_3Sb_5	5.4	10.2
RbV_3Sb_5	6.9	13.8
KV_3Sb_5	26.7	28.5

FIG. 10. An example of fitting for the Raman response in RR (a) and RL (b) scattering geometries at 20 K for CsV_3Sb_5. The red, blue, and green lines represent the total fitted response, the individual Lorentzian components, and a smooth background, respectively.

of these modes.

In Fig. 2, we present the T-dependence of the phonon modes in both RR and RL scattering geometries for CsV_3Sb_5. The main E_{2g} phonon at $119\,cm^{-1}$ and main A_{1g} phonon at $137\,cm^{-1}$ persist across T_S. In contrast, all the new E_{2g} modes abruptly appear below T_S. Most of the new A_{1g} modes first appear as relatively broad features which then sharpen upon cooling.

We fit the Raman spectra shown in Fig. 2 by multi-Lorentzian peaks on a smooth background. Examples of the fits for the Raman response in RR and RL scattering geometries at 20 K are presented in Fig. 10.

In Fig. 11, we show the T-dependence of the phonon frequencies, HWHM, and the integrated intensity for the main E_{2g} phonon at $119\,cm^{-1}$ and main A_{1g} mode at $137\,cm^{-1}$ in CsV_3Sb_5. For the main E_{2g} phonon, the frequency increases upon cooling and shows little changes across T_S. It can be well described by the anharmonic phonon decay model [Appendix F]. The HWHM decreases upon cooling and decreases faster below T_S. The integrated intensity increases slowly upon cooling and stay almost a constant below T_S.

The main A_{1g} phonon hardens upon cooling and shows a large additional hardening below T_S, suggesting the main A_{1g} phonon couples to the A_{1g}-symmetry CDW order parameter below T_S. The main A_{1g} phonon narrows upon cooling and narrows much faster below T_S. The HWHM of this mode starts to decrease slower at a lower temperature $T^* = 70$ K. The T-dependence of HWHM for this mode strongly deviates from the anharmonic phonon decay model [Appendix F], suggesting phononic self-energy effect due to the coupling to the A_{1g}-symmetry CDW order parameter below T_S. The integrated intensity for the main A_{1g} phonon decreases a

bit upon cooling and increases slightly below T_S, which is an indication of finite electron-phonon coupling in this system [66].

3. Temperature dependence of the amplitude modes

In this section, we study the T-dependence of the new A_{1g} and E_{2g} modes. They are both the amplitude modes of the CDW order parameter.

We first discuss the T-dependence of the new A_{1g} amplitude modes. Since each new A_{1g} mode is a doublet [Section III D 3], we fit each new A_{1g} mode with double-Lorentzian functions except for the $45\,cm^{-1}$ mode [Fig. 10(a)].

In Fig. 12, we present the selected T-dependence of peak frequency, HWHM and integrated intensity for the new A_{1g} phonon modes. For the modes at $45\,cm^{-1}$, $202\,cm^{-1}$ and $241\,cm^{-1}$, the T-dependence of these peak frequency and HWHM follow the anharmonic phonon decay model well below T_S [Appendix F]. To the contrary, the T-dependence of the phonon peak frequency and HWHM for the mode at $105\,cm^{-1}$ deviates from the anharmonic phonon decay model in the range $60 \sim 80$ K [Fig. 12(d) and (e)]. Same is found for the mode at $197\,cm^{-1}$ which shows a deviation at around $T^*=70$ K, as shown in Fig. 12(g). These anomalies are consistent with the theoretical T-dependence of the amplitude modes frequencies at around 80 K [Fig. 7(d)], which is close to T^*
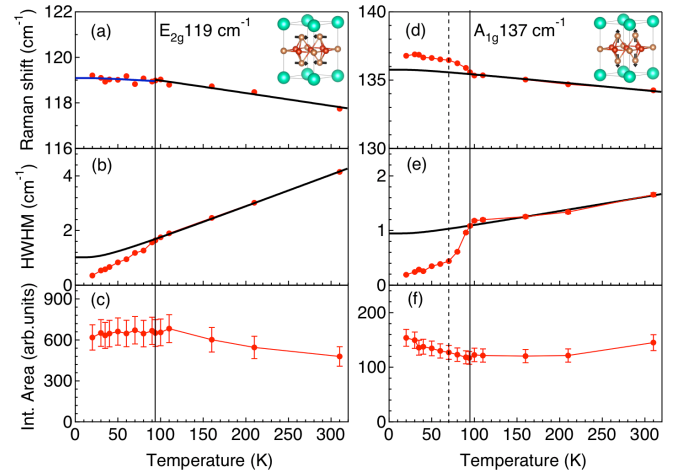

FIG. 11. T-dependence of the peak position (a), HWHM (half width at half maximum) (b) and integrated intensity (c) for the main E_{2g} phonon at $119\,cm^{-1}$ for CsV_3Sb_5. (d)-(f) Same as (a)-(c) but for the main A_{1g} phonon at $137\,cm^{-1}$. The error bars represent one standard deviation. The solid black and blue lines represent the fitting of the phononic self-energy T-dependence above T_S and below T_S by anharmonic decay model, respectively [Eq. F1 and F2]. The solid vertical lines represent T_S while the dashed black lines represent T^*. The insets of (a) and (d) show the lattice vibration patterns for the E_{2g} phonon and A_{1g} phonon, respectively.
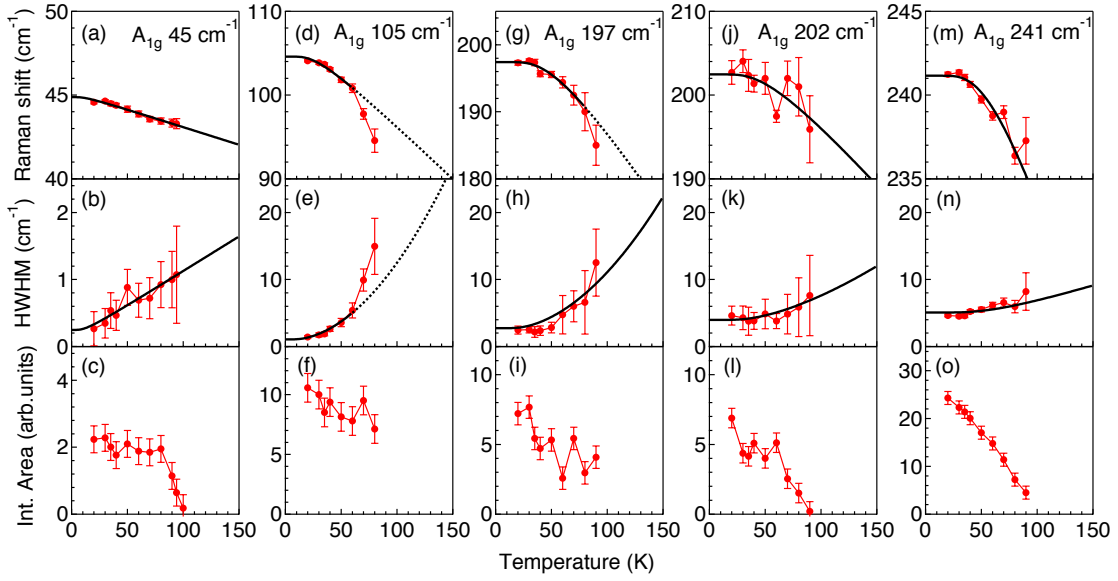
FIG. 12. T-dependence of the peak position, HWHM and integrated intensity for the new A_{1g} phonon mode below T_S for CsV$_3$Sb$_5$. (a)-(c) is for the mode at $45\,\mathrm{cm}^{-1}$. (d)-(f) is for the mode at $105\,\mathrm{cm}^{-1}$. (g)-(i) is for the mode at $197\,\mathrm{cm}^{-1}$. (j)-(l) is for the the mode at $202\,\mathrm{cm}^{-1}$. (m)-(o) is for the mode at $241\,\mathrm{cm}^{-1}$. The error bars represent one standard deviation. For fitting of the phononic self-energy T-dependence for the mode at $45\,\mathrm{cm}^{-1}$ and $241\,\mathrm{cm}^{-1}$, Eq. F1 and Eq. F2 are used; For the modes at $105\,\mathrm{cm}^{-1}$, $197\,\mathrm{cm}^{-1}$, and $202\,\mathrm{cm}^{-1}$, Eq. F3 and F4 are used.

that is set to be $70\,\mathrm{K}$ in the free energy model [Eq. 6]. These anomalies at around T^* results from the interplay between the primary-like and secondary-like order parameters.

The integrated intensity for the new A_{1g} mode at $241\,\mathrm{cm}^{-1}$ increases monotonically below T_S [Fig. 12(o)], indicating a dominant order parameter emerging below T_S. To the contrary, the new A_{1g} mode at $105\,\mathrm{cm}^{-1}$ first appears as a weak and broad feature below T_S, then becomes noticeable at around $T^* = 70\,\mathrm{K}$ and gradually gain intensity below T^* [Fig. 2(b)]. The integrated intensity for this mode shows a saturation-like behavior below T^* [Fig. 12(f)]. Similar behaviors are also found for the modes at $197\,\mathrm{cm}^{-1}$ and $202\,\mathrm{cm}^{-1}$ [Fig. 12(i) and (l)]. These results suggest that a secondary order parameter comes into play below T^*.

The above two different behaviors for the A_{1g} modes' integrated intensity –the monotonical increase and the saturation-like behavior– can be captured by the Landau free energy model [Eq. 6] incorporating the interplay between the primary-like (u_0) and the secondary-like (l_0) order parameters via trilinear coupling $\gamma u_0^2 l_0$. The plateau-like behavior for the A_{1g} mode at $105\,\mathrm{cm}^{-1}$ below T^* can be modeled by the T-dependence of $(u_0+l_0)^2$ in the case of $\gamma > 0$ where u_0 and l_0 have different signs. In this case, u_0 and l_0 interplay with each other destructively, thus $(u_0+l_0)^2$ shows a plateau-like behavior below T^* [Fig. 7(e)]. The monotonic increase of the integrated intensity for the higher-energy A_{1g} modes at $241\,\mathrm{cm}^{-1}$ can be qualitatively described by the T-dependence of the $(u_0+l_0)^2$ in the case of $\gamma < 0$ where u_0 and l_0 have

the same signs. In this case, u_0 and l_0 interplay with each other constructively, thus $(u_0+l_0)^2$ increases monotonically below T_S [Fig. 7(f)].

The above two different behaviors for the integrated intensities originate from the multiband nature of AV$_3$Sb$_5$. Recent angle-resolved photoemission measurements indeed revealed that multiple V $3d$ bands cross the Fermi level [35, 38, 62, 63]. The Landau free energy parameters, especially the trilinear coupling constant γ, vary for different bands. They determine whether the primary-like U_1 and secondary-like L_2^- order parameters interplay constructively or destructively, thus determining the shape of the T-dependence of the integrated intensity below T_S.

We note that the appearance of the A_{1g} mode at $105\,\mathrm{cm}^{-1}$ below T^* was also reported in the ultrafast coherent phonon spectroscopy measurements [37–39]. The authors of these works [37–39] linked the temperature T^* to the emergence of a uniaxial charge modulation observed by STM [15, 16, 22], which breaks both C_6/C_3 rotational symmetry. However, the presented here x-ray and Raman data do not support this scenario. First, both x-ray and Raman results indicate that C_3 rotational symmetry is preserved in the CDW ground state. Secondly, the Raman data shown in Fig. 2 do not show any additional sets of new phonon modes below T^*. Third, the refined low-temperature structure shown in Fig. 6 does not contain an interlayer π phase shift, ruling out the bulk D_{2h} $2 \times 2 \times 2$ CDW order [67]. Thus, the presented here results suggest that the uniaxial charge modulation below T^* is not a bulk effect.
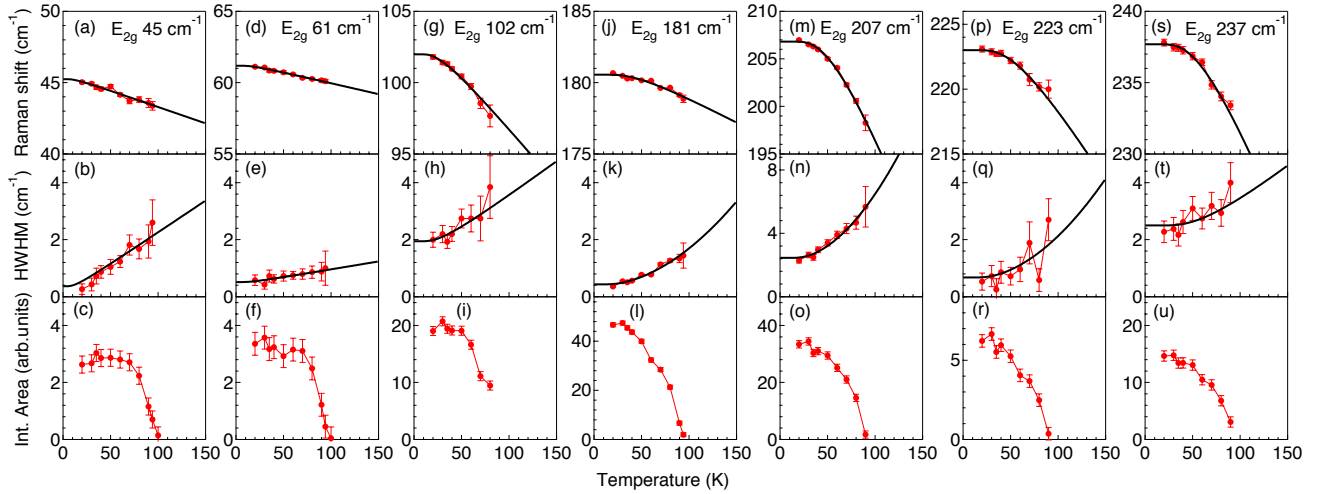
FIG. 13. T-dependence of the peak position, HWHM and integrated intensity for the new E_{2g} phonon modes below T_S for CsV$_3$Sb$_5$. (a)-(c) is for the mode at $45\,\text{cm}^{-1}$. (d)-(f) is for the mode at $61\,\text{cm}^{-1}$. (g)-(i) is for the mode at $102\,\text{cm}^{-1}$. (j)-(l) is for the mode at $181\,\text{cm}^{-1}$. (m)-(o) is for the mode at $207\,\text{cm}^{-1}$. (p)-(r) is for the mode at $223\,\text{cm}^{-1}$. (s)-(u) is for the mode at $237\,\text{cm}^{-1}$. The error bars represent one standard deviation. For fitting of the phononic self-energy T-dependence for the modes at $45\,\text{cm}^{-1}$, $61\,\text{cm}^{-1}$, and $102\,\text{cm}^{-1}$, Eq. F1 and Eq. F2 are used; For the modes at $181\,\text{cm}^{-1}$, $207\,\text{cm}^{-1}$, and $223\,\text{cm}^{-1}$, Eq. F1 and F2 are used.

Finally, we switch to discuss the T-dependence of the E_{2g} modes, which are accessed spectroscopically by exciting the amplitude modes of the "failed order parameters". In Fig. 13, we present the T-dependence of the new E_{2g} phonon modes. In general, the T-dependence of peak frequency and HWHM are smooth, showing no anomalies below T_S. They follow the anharmonic phonon decay model well below T_S [Appendix F]. The abrupt appearance of the new E_{2g} phonon modes below T_S can be clearly seen from the T-dependence of the integrated intensities. They onset at T_S and increase monotonically below T_S, except for the low-energy E_{2g} mode at $61\,\text{cm}^{-1}$. The integrated intensity for this mode shows a saturation-like behavior below $T^*=70\,\text{K}$. These two distinct behaviors are similar to the temperature dependence of the A_{1g} amplitude modes shown in Fig. 12, consistent with the primary-like and secondary-like order parameters.

IV. CONCLUSION

In summary, we study the primary and secondary order parameters associated with the CDW transition in kagome metal AV$_3$Sb$_5$ system by polarization-resolved electronic Raman spectroscopy and DFT calculations.

Previous x-ray diffraction data at $15\,\text{K}$ established that the CDW order in CsV$_3$Sb$_5$ is a $2\times2\times4$ structure with space group $P\bar{3}$: one layer of iSoD structure, and three consecutive layers of SoD structure with zero-phase-shift between neighboring layers. This $2\times2\times4$ structure can be further refined to space group $P6/mmm$ if we disregard the tiny distortions. The Vanadium atoms show

major displacements in the iSoD layer while they show minor displacements in the SoD layer. By quantitatively analyzing the Vanadium lattice distortions, we identify that U_1 lattice distortion is the primary-like order parameter while M_1^+ and L_2^- distortions are secondary-like order parameters. This is also confirmed by the calculation of bare static susceptibility $\chi_0'(q)$ that shows a broad peak at around $q_z = 0.25$ along the hexagonal Brillouin zone face central line (U-line).

The primary and secondary order parameters are revealed by Raman scattering. We identify several A_{1g} and E_{2g} phonon modes related to V and Sb atoms as well as alkali atoms emerging in the CDW state. The symmetry decompositions analysis for these V-and-Sb-atoms-related modes indicates the C_3 symmetry is preserved in the CDW phase. To the contrary, the low-energy alkali-atom-related lattice vibration modes do not obey the D_{6h}-point-group selection rules. These alkali phonon modes indicates a "nematic"-like C_3-symmetry broken phase characterized by the "failed order parameter" with Γ_5^+ (E_{2g}) symmetry that is stabilized on the surface.

The observed number of Raman-active phonon modes in the CDW state indicates that the inversion symmetry remains intact. By comparing the DFT phonon calculations and the observed new phonon frequencies, we find that the $2\times2\times4$ structure hosts a dominant iSoD-type lattice distortion, consistent with the x-ray refinement results.

The detailed temperature evolution of these new modes' peak frequency, HWHM, and integrated intensity support two successive phase transitions in CsV$_3$Sb$_5$: the first one associated with the primary-like order parameter

appearing at $T_S = 94\,$K and the second isostructural one appearing at $T^* = 70\,$K. Moreover, the T-dependence of the integrated intensity for these modes show two type of behavior below T_S: a plateau-like behavior below T^* and monotonically increase below T_S. These two behaviors are captured by a Landau free energy model incorporating the interplay between the primary-like and the secondary-like order parameters via trilinear coupling. Especially, the sign of the trilinear term determine whether the primary-like and secondary-like order parameters cooperate or compete with each other, thus determining the shape of the T-dependence of the Raman data below T_S.

These results establish a solid foundation to study the interplay between the primary and secondary CDW order parameters in kagome metal system. They guide to identify the primary and secondary order parameters as well as their interplay, when these CDW order parameters are tuned by carrier doping [26–28], external pressure [24, 25], or strain [68].

Appendix A: Laser heating determination

The laser heating rate, a measure of the temperature increase per unit laser power (K/mW) in the focused laser spot, in the Raman experiments was determined by monitoring the appearance of new phonon modes induced by the CDW order during the cooling process with a constant laser power $10\,$mW.

At the cryostat temperature $90\,$K, we barely detect any new phonon modes, indicating the laser spot temperature is above $T_S = 94\,$K. When cooling the sample to $85\,$K, we start to detect several weak new phonon signals both in the RR and RL scattering geometries, indicating the laser spot temperature is slightly below $94\,$K. When cooling the sample to $80\,$K, the intensity of these new modes

develop significantly, indicating the laser spot temperature is well below $94\,$K. Thus, the heating coefficient can be determined via: $85 + 10 * k \approx 94$. In this way, we have deduced the heating coefficient: $k \approx 0.9 \pm 0.1\,$K/mW.

Appendix B: Removal of polarization leakage

In this section, we provide the detailed procedure to remove the polarization leakage signal from optical elements in our data analysis.

In our polarization optics setup, we used a Glan-Taylor polarizing prism (Melles Griot) with a extinction ratio better than 10^{-5} to clean the laser excitation beam and a broad-band $50\,$mm polarizing cube (Karl Lambrecht Corporation) with an extinction ratio better than 1:500 to analyze the scattered light. For the linearly polarized XX and XY scatting geometries, the leakage intensity ratio is negligibly small (less than $0.2\,\%$), thus the leakage intensity from the linearly polarized scattering geometries is not considered.

For measurements with circularly polarized light, we employed a Berek compensator (New Focus) to convert the incoming linearly polarized light into circularly polarized light for excitation. We used a broad-band 50-mm-diameter quarter wave retarder (Melles Griot) with a retardance tolerance $\lambda/50$ before the polarizing cube to convert the out-coming circularly polarized light into linearly polarized light for the analyzer. The leakage of circular polarized light is due to the limitations of the broadband quarter wave plate and alignment of the Berek compensator.

The amount of phonon leakage intensity are determined based on the A_{1g} and E_{2g} bulk phonons of CsV_3Sb_5 at the same temperature in RR and RL scattering geometries. To remove the polarization leakage intensity, we subtract intensity from the orthogonal polarization geometry, i.e., $\chi''_{RR}(\omega, T) = \overline{\chi''_{RR}}(\omega, T) - \alpha \cdot \overline{\chi''_{RL}}(\omega, T)$, where $\overline{\chi''_{RR}}(\omega, T)$ and $\overline{\chi''_{RL}}(\omega, T)$ are the raw data taken in RR and RL polarization scattering geometries at temperature T, respectively, and α is a small number representing the leakage ratio. It is expected that the same ratio α also applies to RL polarization scattering geometry as well: $\chi''_{RL}(\omega, T) = \overline{\chi''_{RL}}(\omega, T) - \alpha \cdot \overline{\chi''_{RR}}(\omega, T)$.

In Fig. 14, we show the Raman spectra of the unprocessed raw data and polarization-leakage-removed spectra taken at $60\,$K from the ab surface of CsV_3Sb_5 crystals in RR and RL scattering geometries, respectively. The leakage intensity of the bulk E_{2g} phonons at $119\,$cm^{-1} and $181\,$cm^{-1} in the raw data taken with RR scattering geometries can be fully removed with a leakage ratio α close to 0.02.
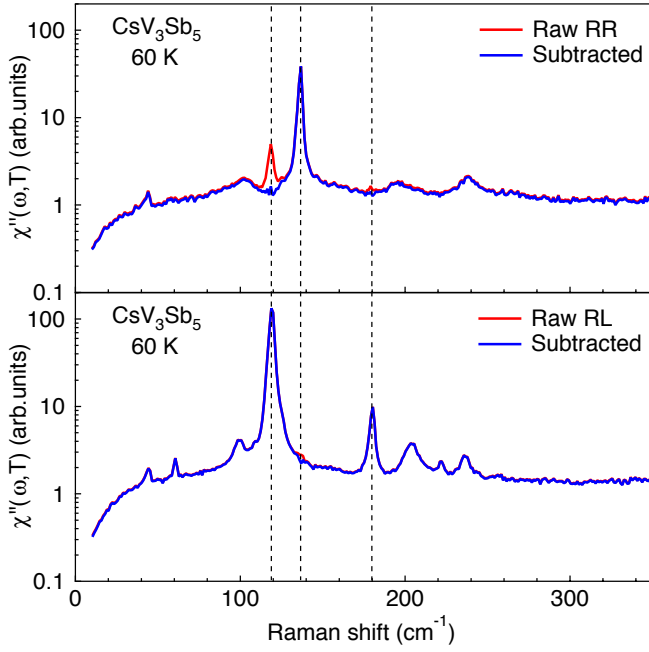
FIG. 14. Comparison of raw data and polarization leakage removed spectra, taken in RR (top panel) and RL (bottom panel) polarization scattering geometry from the ab surface of CsV_3Sb_5 at 60 K with 647 nm laser excitation.

Appendix C: Raman tensor analysis

The Raman tensor R_μ is a 2×2 matrix for an irreducible representation (μ) of a point group. It can be used to estimate the phonon intensity in a Raman experiment. With incident and scattering light polarization unit vector respectively defined as $\hat{e}_i$ and $\hat{e}_s$, the phononic Raman response is described as [69]:

$$\chi''_{\hat{e}_i \hat{e}_s} \sim \sum_\mu |\hat{e}_i R_\mu \hat{e}_s|^2. \qquad (C1)$$

The Raman tensors R_μ ($\mu = A_{1g}, A_{2g}, E_{1g}, E_{2g}$) for the irreducible representations (μ) of point group D_{6h} have the following forms:

$$\begin{pmatrix} a & 0 & 0 \\ 0 & a & 0 \\ 0 & 0 & b \end{pmatrix}, \begin{pmatrix} 0 & c & 0 \\ -c & 0 & 0 \\ 0 & 0 & 0 \end{pmatrix}, \begin{pmatrix} 0 & 0 & 0 \\ 0 & 0 & d \\ 0 & e & 0 \end{pmatrix} \begin{pmatrix} 0 & 0 & -d \\ 0 & 0 & 0 \\ -e & 0 & 0 \end{pmatrix},$$

$$\begin{pmatrix} 0 & f & 0 \\ f & 0 & 0 \\ 0 & 0 & 0 \end{pmatrix} \begin{pmatrix} f & 0 & 0 \\ 0 & -f & 0 \\ 0 & 0 & 0 \end{pmatrix}.$$

We choose $\hat{e}_i$ and $\hat{e}_s$ to be X, Y, R, and L, where $X = (1\ 0\ 0)$, $Y = (0\ 1\ 0)$, $R = 1/\sqrt{2}\ (1\ i\ 0)$, and $L = 1/\sqrt{2}\ (1\ -i\ 0)$.
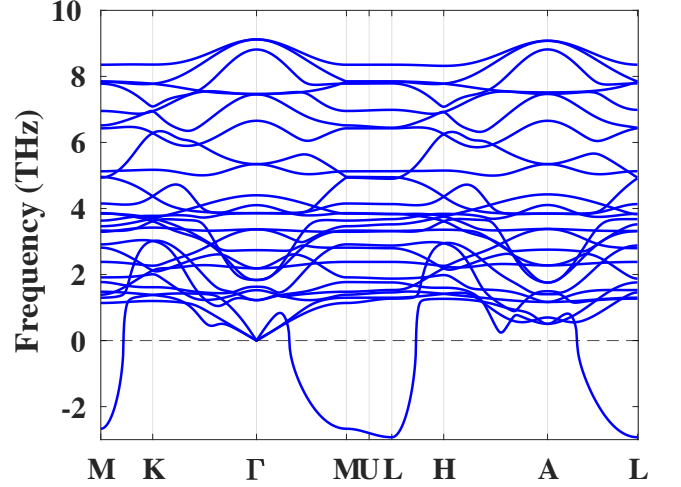

FIG. 15. DFT calculation of phonon dispersion in the whole Brillouin zone for the high-temperature phase of CsV_3Sb_5.

Based on Eq. C1, we obtain:

$$\begin{aligned} \chi''^{D_{6h}}_{XX} &= a^2 + f^2, \\ \chi''^{D_{6h}}_{XY} &= c^2 + f^2, \\ \chi''^{D_{6h}}_{RR} &= a^2 + c^2, \\ \chi''^{D_{6h}}_{RL} &= 2f^2. \end{aligned} \qquad (C2)$$

Thus, the Raman selection rules for the D_{6h} point group indicate that the XX, XY, RR, and RL polarization geometries probe the $A_{1g} + E_{2g}$, $A_{2g} + E_{2g}$, $A_{1g} + A_{2g}$, $2E_{2g}$ symmetry excitations, respectively [Table I].

The sum rule that $\chi''^{D_{6h}}_{XX} + \chi''^{D_{6h}}_{XY} = \chi''^{D_{6h}}_{RR} + \chi''^{D_{6h}}_{RL} = a^2 + c^2 + 2f^2$ set a constraint for the Raman response in different scattering geometries, thus providing a unique way to check the data consistency.

From Eq. C2, we can calculate the square of the Raman tensor element:

$$\begin{aligned} a^2 &= \chi''^{D_{6h}}_{XX} - \chi''^{D_{6h}}_{RL}/2, \\ c^2 &= \chi''^{D_{6h}}_{XY} - \chi''^{D_{6h}}_{RL}/2, \\ f^2 &= \chi''^{D_{6h}}_{RL}/2. \end{aligned} \qquad (C3)$$

Therefore, the algebra Eq. C3 can be used to decompose the measured Raman signal into three separate irreducible representations (A_{1g}, A_{2g}, E_{2g}) of point group D_{6h} [Table II].

This decomposition algebra is a characteristic property of a lattice system with trigonal or hexagonal symmetries where the three-fold rotational symmetry is preserved [70].

Appendix D: Phonon instability calculation

In Fig. 15, we show DFT calculation of the phonon frequencies in the whole Brillouin zone for the high-

temperature phase of CsV_3Sb_5. The lowest phonon branch shows a broad imaginary response along the whole U line [M-U-L line], as well as the ΓM and AL lines. Therefore, the DFT calculation does not provide a unique identification of the lattice instability vector.

Appendix E: Group theoretical analysis

In this section, we focus on the folded phonon modes in the BZ center which originate from BZ boundary due to the CDW ordering.

Extending the high-temperature supercell to the $2 \times 2 \times 1$ supercell, we have two types of CDW order driven by V displacements in the kagome layer: SoD and iSoD structure. These two superlattice share the same space group of $P6/mmm$ as the high-temperature phase, displaying an in-plane 2×2 modulation of the high-temperature structure. From the group theoretical considerations [71], Γ point phonon modes of the $2 \times 2 \times 1$ supercell can be expressed as $\Gamma_{\text{total}} = 5A_{1g} + A_{1u} + 3A_{2g} + 9A_{2u} + 4B_{1g} + 5B_{1u} + 2B_{2g} + 7B_{2u} + 8E_{2u} + 8E_{2g} + 14E_{1u} + 6E_{1g}$. Raman active modes $\Gamma_{\text{Raman}} = 5A_{1g} + 8E_{2g} + 6E_{1g}$, IR active modes are $\Gamma_{\text{IR}} = 8A_{2u} + 13E_{1u}$, the acoustic mode $\Gamma_{\text{acoustic}} = A_{2u} + E_{1u}$ and the silent modes are $\Gamma_{\text{silent}} = 3A_{2g} + 4B_{1g} + 2B_{2g} + A_{1u} + 5B_{1u} + 7B_{2u} + 8E_{2u}$. Note that alkali atoms (K, Rb, Cs) do not involve any Raman-active vibration in the $2 \times 2 \times 1$ SoD and iSoD phase, as well as in the high-temperature phase.

Extending the $2 \times 2 \times 1$ supercell to the three dimensional $2 \times 2 \times 4$ supercell, we have a structure composed of one layer of the iSoD structures and three consecutive layers of SoD structure, with zero-phase-shift between neighboring layers [Fig. 6]. It has the same space group $P6/mmm$ as the high-temperature phase. From the group theoretical considerations, Γ point phonon modes of this superstructure can be expressed as $\Gamma_{\text{total}} = 26A_{1g} + 6A_{1u} + 10A_{2g} + 30A_{2u} + 20B_{1g} + 16B_{1u} + 12B_{2g} + 24B_{2u} + 31E_{2u} + 33E_{2g} + 45E_{1u} + 35E_{1g}$, where Raman active modes $\Gamma_{\text{Raman}} = 26A_{1g} + 33E_{2g} + 35E_{1g}$, IR active modes are $\Gamma_{\text{IR}} = 29A_{2u} + 44E_{1u}$, the acoustic mode $\Gamma_{\text{acoustic}} = A_{2u} + E_{1u}$ and the silent modes are $\Gamma_{\text{silent}} = 6A_{1u} + 10A_{2g} + 20B_{1g} + 16B_{1u} + 12B_{2g} + 24B_{2u} + 31E_{2u}$. Note that the alkali atoms (Cs, Rb, K) lattice vibrations become Raman-active in the $2 \times 2 \times 4$ superstructure.

Appendix F: Anharmonic phonon decay model

In this section, we discuss the anharmonic phonon decay model. We fit the temperature dependence of the phonon frequency and HWHM by anharmonic phonon decay model [72, 73]:

$$\omega_1(T) = \omega_0 - C_1 \left[1 + 2n(\Omega(T)/2)\right], \qquad \text{(F1)}$$

$$\Gamma_1(T) = \gamma_0 + \gamma_1 \left[1 + 2n(\Omega(T)/2)\right], \qquad \text{(F2)}$$

$$\omega_2(T) = \omega_1(T) - C_2 \left[1 + 3n(\Omega(T)/3) + 3n^2(\Omega(T)/3)\right], \qquad \text{(F3)}$$

$$\Gamma_2(T) = \Gamma_1(T) + \gamma_2 \left[1 + 3n(\Omega(T)/3) + 3n^2(\Omega(T)/3)\right], \qquad \text{(F4)}$$

where $\Omega(T) = \hbar\omega/k_B T$, $n(x) = 1/(e^x - 1)$ is the Bose-Einstein distribution function. $\omega_1(T)$ and $\Gamma_1(T)$ involves mainly three-phonon decay process where an optical phonon decays into two acoustic modes with equal energy and opposite momentum. $\omega_2(T)$ and $\Gamma_2(T)$ involves additional four-phonon decay processes compared with $\omega_1(T)$ and $\Gamma_1(T)$.

[1] I. Syôzi, Statistics of Kagome Lattice, Progress of Theoretical Physics **6**, 306 (1951).

[2] C. Broholm, R. J. Cava, S. A. Kivelson, D. G. Nocera, M. R. Norman, and T. Senthil, Quantum spin liquids, Science **367**, eaay0668 (2020).

[3] W.-S. Wang, Z.-Z. Li, Y.-Y. Xiang, and Q.-H. Wang, Competing electronic orders on Kagome lattices at van Hove filling, Phys. Rev. B **87**, 115135 (2013).

[4] M. L. Kiesel, C. Platt, and R. Thomale, Unconventional Fermi surface instabilities in the Kagome Hubbard model, Phys. Rev. Lett. **110**, 126405 (2013).

[5] X. Feng, K. Jiang, Z. Wang, and J. Hu, Chiral flux phase in the Kagome superconductor AV$_3$Sb$_5$, Science Bulletin **66**, 1384 (2021).

[6] M. M. Denner, R. Thomale, and T. Neupert, Analysis of charge order in the kagome metal av$_3$sb$_5$ (a = K, Rb, Cs), Phys. Rev. Lett. **127**, 217601 (2021).

[7] Y.-P. Lin and R. M. Nandkishore, Complex charge density waves at Van Hove singularity on hexagonal lattices: Haldane-model phase diagram and potential realization in the kagome metals AV_3Sb_5 (A=K, Rb, Cs), Phys. Rev. B **104**, 045122 (2021).

[8] T. Park, M. Ye, and L. Balents, Electronic instabilities of kagome metals: saddle points and Landau theory, Phys. Rev. B **104**, 035142 (2021).

[9] C. Setty, H. Hu, L. Chen, and Q. Si, Electron correlations and T-breaking density wave order in a Z_2 Kagome metal , arXiv:2105.15204 (2021).

[10] X. Feng, Y. Zhang, K. Jiang, and J. Hu, Low-energy effective theory and symmetry classification of flux phases on the kagome lattice, Phys. Rev. B **104**, 165136 (2021).

[11] M. H. Christensen, T. Birol, B. M. Andersen, and R. M. Fernandes, Theory of the charge density wave in AV_3Sb_5 kagome metals, Phys. Rev. B **104**, 214513 (2021).

[12] R. Tazai, Y. Yamakawa, S. Onari, and H. Kontani, Mechanism of exotic density-wave and beyond-Migdal unconventional superconductivity in kagome metal AV$_3$Sb$_5$ (A=K, Rb, Cs), arXiv:2107.05372 (2021).

[13] K. Jiang, T. Wu, J.-X. Yin, Z. Wang, M. Z. Hasan, S. D. Wilson, X. Chen, and J. Hu, Kagome superconductors AV$_3$Sb$_5$ (A=K, Rb, Cs), arXiv:2109.10809 (2021).

[14] Y. Xie, Y. Li, P. Bourges, A. Ivanov, Z. Ye, J.-X. Yin, M. Z. Hasan, A. Luo, Y. Yao, Z. Wang, G. Xu, and P. Dai, Electron-phonon coupling in the charge density wave state of CsV$_3$Sb$_5$, arXiv:2111.00654 (2021).

[15] H. Chen, H. Yang, B. Hu, Z. Zhao, J. Yuan, Y. Xing, G. Qian, Z. Huang, G. Li, Y. Ye, S. Ma, S. Ni, H. Zhang, Q. Yin, C. Gong, Z. Tu, H. Lei, H. Tan, S. Zhou, C. Shen, X. Dong, B. Yan, Z. Wang, and H.-J. Gao, Roton pair density wave in a strong-coupling kagome superconductor, Nature 599, 222 (2021).

[16] Z. Liang, X. Hou, F. Zhang, W. Ma, P. Wu, Z. Zhang, F. Yu, J.-J. Ying, K. Jiang, L. Shan, Z. Wang, and X.-H. Chen, Three-dimensional charge density wave and surface-dependent vortex-core states in a kagome superconductor CsV$_3$Sb$_5$, Phys. Rev. X 11, 031026 (2021).

[17] B. R. Ortiz, L. C. Gomes, J. R. Morey, M. Winiarski, M. Bordelon, J. S. Mangum, I. W. H. Oswald, J. A. Rodriguez-Rivera, J. R. Neilson, S. D. Wilson, E. Ertekin, T. M. McQueen, and E. S. Toberer, New Kagome prototype materials: discovery of KV$_3$Sb$_5$, RbV$_3$Sb$_5$, and CsV$_3$Sb$_5$, Phys. Rev. Materials 3, 094407 (2019).

[18] B. R. Ortiz, S. M. L. Teicher, Y. Hu, J. L. Zuo, P. M. Sarte, E. C. Schueller, A. M. M. Abeykoon, M. J. Krogstad, S. Rosenkranz, R. Osborn, R. Seshadri, L. Balents, J. He, and S. D. Wilson, CsV$_3$Sb$_5$: a $\mathbb{Z}_2$ topological kagome metal with a superconducting ground state, Phys. Rev. Lett. 125, 247002 (2020).

[19] B. R. Ortiz, P. M. Sarte, E. M. Kenney, M. J. Graf, S. M. L. Teicher, R. Seshadri, and S. D. Wilson, Superconductivity in the $\mathbb{Z}_2$ Kagome metal KV$_3$Sb$_5$, Phys. Rev. Materials 5, 034801 (2021).

[20] Y.-X. Jiang, J.-X. Yin, M. M. Denner, N. Shumiya, B. R. Ortiz, G. Xu, Z. Guguchia, J. He, M. S. Hossain, X. Liu, J. Ruff, L. Kautzsch, S. S. Zhang, G. Chang, I. Belopolski, Q. Zhang, T. A. Cochran, D. Multer, M. Litskevich, Z.-J. Cheng, X. P. Yang, Z. Wang, R. Thomale, T. Neupert, S. D. Wilson, and M. Z. Hasan, Unconventional chiral charge order in kagome superconductor KV$_3$Sb$_5$, Nature Materials 20, 1353 (2021).

[21] H. Tan, Y. Liu, Z. Wang, and B. Yan, Charge density waves and electronic properties of superconducting kagome metals, Phys. Rev. Lett. 127, 046401 (2021).

[22] H. Zhao, H. Li, B. R. Ortiz, S. M. L. Teicher, T. Park, M. Ye, Z. Wang, L. Balents, S. D. Wilson, and I. Zeljkovic, Cascade of correlated electron states in the kagome superconductor CsV$_3$Sb$_5$, Nature 599, 216 (2021).

[23] H. Li, T. T. Zhang, T. Yilmaz, Y. Y. Pai, C. E. Marvinney, A. Said, Q. W. Yin, C. S. Gong, Z. J. Tu, E. Vescovo, C. S. Nelson, R. G. Moore, S. Murakami, H. C. Lei, H. N. Lee, B. J. Lawrie, and H. Miao, Observation of unconventional charge density wave without acoustic phonon anomaly in Kagome superconductors AV$_3$Sb$_5$ (A = Rb, Cs), Phys. Rev. X 11, 031050 (2021).

[24] K. Y. Chen, N. N. Wang, Q. W. Yin, Y. H. Gu, K. Jiang, Z. J. Tu, C. S. Gong, Y. Uwatoko, J. P. Sun, H. C. Lei, J. P. Hu, and J.-G. Cheng, Double superconducting dome and triple enhancement of T_c in the Kagome superconductor CsV$_3$Sb$_5$ under high pressure, Phys. Rev. Lett. 126, 247001 (2021).

[25] F. H. Yu, D. H. Ma, W. Z. Zhuo, S. Q. Liu, X. K. Wen, B. Lei, J. J. Ying, and X. H. Chen, Unusual competition of superconductivity and charge-density-wave state

[26] in a compressed topological kagome metal, Nat. Commun. 12, 3645 (2021).

[26] Y. M. Oey, B. R. Ortiz, F. Kaboudvand, J. Frassineti, E. Garcia, S. Sanna, V. Mitrovi, R. Seshadri, and S. D. Wilson, Fermi level tuning and double-dome superconductivity in the kagome metals CsV$_3$Sb$_{5-x}$Snx, arXiv:2110.10912 (2021).

[27] Y. Liu, Y. Wang, Y. Cai, Z. Hao, X.-M. Ma, L. Wang, C. Liu, J. Chen, L. Zhou, J. Wang, S. Wang, H. He, Y. Liu, S. Cui, J. Wang, B. Huang, C. Chen, and J.-W. Mei, Doping evolution of superconductivity, charge order and band topology in hole-doped topological kagome superconductors Cs(V$_{1-x}$Ti$_x$)$_3$Sb$_5$, arXiv:2110.12651 (2021).

[28] Y. Song, T. Ying, X. Chen, X. Han, X. Wu, A. P. Schnyder, Y. Huang, J.-g. Guo, and X. Chen, Competition of superconductivity and charge density wave in selective oxidized CsV$_3$Sb$_5$ thin flakes, Phys. Rev. Lett. 127, 237001 (2021).

[29] B. Q. Song, X. M. Kong, W. Xia, Q. W. Yin, C. P. Tu, C. C. Zhao, D. Z. Dai, K. Meng, Z. C. Tao, Z. J. Tu, C. S. Gong, H. C. Lei, Y. F. Guo, X. F. Yang, and S. Y. Li, Competing superconductivity and charge-density wave in kagome metal CsV$_3$Sb$_5$: evidence from their evolutions with sample thickness, arXiv:2105.09248 (2021).

[30] S.-Y. Yang, Y. Wang, B. R. Ortiz, D. Liu, J. Gayles, E. Derunova, R. Gonzalez-Hernandez, L. mejkal, Y. Chen, S. S. P. Parkin, S. D. Wilson, E. S. Toberer, T. McQueen, and M. N. Ali, Giant, unconventional anomalous Hall effect in the metallic frustrated magnet candidate, KV$_3$Sb$_5$, Sci. Adv. 6, eabb6003 (2020).

[31] F. H. Yu, T. Wu, Z. Y. Wang, B. Lei, W. Z. Zhuo, J. J. Ying, and X. H. Chen, Concurrence of anomalous hall effect and charge density wave in a superconducting topological kagome metal, Phys. Rev. B 104, L041103 (2021).

[32] E. M. Kenney, B. R. Ortiz, C. Wang, S. D. Wilson, and M. J. Graf, Absence of local moments in the kagome metal KV$_3$Sb$_5$ as determined by muon spin spectroscopy, J. Phys. Condens. Matter 33, 235801 (2021).

[33] C. Mielke, D. Das, J.-X. Yin, H. Liu, R. Gupta, Y.-X. Jiang, M. Medarde, X. Wu, H. C. Lei, J. Chang, P. Dai, Q. Si, H. Miao, R. Thomale, T. Neupert, Y. Shi, R. Khasanov, M. Z. Hasan, H. Luetkens, and Z. Guguchia, Time-reversal symmetry-breaking charge order in a kagome superconductor, Nature 602, 245 (2022).

[34] L. Yu, C. Wang, Y. Zhang, M. Sander, S. Ni, Z. Lu, S. Ma, Z. Wang, Z. Zhao, H. Chen, K. Jiang, Y. Zhang, H. Yang, F. Zhou, X. Dong, S. L. Johnson, M. J. Graf, J. Hu, H.-J. Gao, and Z. Zhao, Evidence of a hidden flux phase in the topological kagome metal CsV$_3$Sb$_5$, arXiv:2107.10714 (2021).

[35] H. Luo, Q. Gao, H. Liu, Y. Gu, D. Wu, C. Yi, J. Jia, S. Wu, X. Luo, Y. Xu, L. Zhao, Q. Wang, H. Mao, G. Liu, Z. Zhu, Y. Shi, K. Jiang, J. Hu, Z. Xu, and X. J. Zhou, Electronic nature of charge density wave and electron-phonon coupling in kagome superconductor KV$_3$Sb$_5$, Nature Communications 13, 273 (2022).

[36] B. R. Ortiz, S. M. L. Teicher, L. Kautzsch, P. M. Sarte, N. Ratcliff, J. Harter, J. P. C. Ruff, R. Seshadri, and S. D. Wilson, Fermi Surface Mapping and the Nature of Charge-Density-Wave Order in the Kagome Superconductor CsV$_3$Sb$_5$, Phys. Rev. X 11, 041030 (2021).

[37] N. Ratcliff, L. Hallett, B. R. Ortiz, S. D. Wilson, and J. W. Harter, Coherent phonon spectroscopy and interlayer modulation of charge density wave order in the kagome metal CsV_3Sb_5, Phys. Rev. Materials **5**, L111801 (2021).

[38] Z. X. Wang, Q. Wu, Q. W. Yin, C. S. Gong, Z. J. Tu, T. Lin, Q. M. Liu, L. Y. Shi, S. J. Zhang, D. Wu, H. C. Lei, T. Dong, and N. L. Wang, Unconventional charge density wave and photoinduced lattice symmetry change in the kagome metal CsV_3Sb_5 probed by time-resolved spectroscopy, Phys. Rev. B **104**, 165110 (2021).

[39] Q. Wu, Z. X. Wang, Q. M. Liu, R. S. Li, S. X. Xu, Q. W. Yin, C. S. Gong, Z. J. Tu, H. C. Lei, T. Dong, and N. L. Wang, The large static and pump-probe Kerr effect with two-fold rotation symmetry in Kagome metal CsV_3Sb_5, arXiv:2110.11306 (2021).

[40] S. Ni, S. Ma, Y. Zhang, J. Yuan, H. Yang, Z. Lu, N. Wang, J. Sun, Z. Zhao, D. Li, S. Liu, H. Zhang, H. Chen, K. Jin, J. Cheng, L. Yu, F. Zhou, X. Dong, J. Hu, H.-J. Gao, and Z. Zhao, Anisotropic superconducting properties of Kagome metal CsV_3Sb_5, Chinese Physics Letters **38**, 057403 (2021).

[41] Y. Xiang, Q. Li, Y. Li, W. Xie, H. Yang, Z. Wang, Y. Yao, and H.-H. Wen, Twofold symmetry of c-axis resistivity in topological kagome superconductor CsV_3Sb_5 with in-plane rotating magnetic field, Nat. Commun **12**, 6727 (2021).

[42] J. P. Perdew, K. Burke, and M. Ernzerhof, Generalized gradient approximation made simple, Phys. Rev. Lett. **77**, 3865 (1996).

[43] G. Kresse and J. Furthmüller, Efficient iterative schemes for ab initio total-energy calculations using a plane-wave basis set, Phys. Rev. B **54**, 11169 (1996).

[44] G. Kresse and J. Furthmller, Efficiency of ab-initio total energy calculations for metals and semiconductors using a plane-wave basis set, Computational Materials Science **6**, 15 (1996).

[45] A. Togo and I. Tanaka, First principles phonon calculations in materials science, Scripta Materialia **108**, 1 (2015).

[46] M. D. Johannes and I. I. Mazin, Fermi surface nesting and the origin of charge density waves in metals, Phys. Rev. B **77**, 165135 (2008).

[47] A. A. Mostofi, J. R. Yates, Y.-S. Lee, I. Souza, D. Vanderbilt, and N. Marzari, wannier90: A tool for obtaining maximally-localised Wannier functions, Computer Physics Communications **178**, 685 (2008).

[48] B. J. Campbell, H. T. Stokes, D. E. Tanner, and D. M. Hatch, *ISODISPLACE*: a web-based tool for exploring structural distortions, Journal of Applied Crystallography **39**, 607 (2006).

[49] A. P. Cracknell, B. L. Davies, S. C. Miller, and W. F. Love, Kronecker Product Tables. Vol. 1. General introduction and Tables of irreducible representations of space groups (IFI/Plenum, New York, 1979).

[50] M. I. Aroyo, J. M. Perez-Mato, D. Orobengoa, E. Tasci, G. De La Flor, and A. Kirov, Crystallography online: Bilbao crystallographic server, Bulg. Chem. Commun **43**, 183 (2011).

[51] M. I. Aroyo, A. Kirov, C. Capillas, J. M. Perez-Mato, and H. Wondratschek, Bilbao crystallographic server. ii. representations of crystallographic point groups and space groups, Acta Crystallogr., Sect A: Found. Crystallogr. **62**, 115 (2006).

[52] C. Wang, S. Liu, H. Jeon, and J.-H. Cho, Origin of charge density wave in the layered kagome metal CsV_3Sb_5, Phys. Rev. B **105**, 045135 (2022).

[53] M. D. Johannes, I. I. Mazin, and C. A. Howells, Fermi-surface nesting and the origin of the charge-density wave in $NbSe_2$, Phys. Rev. B **73**, 205102 (2006).

[54] The reason that we do not regard the U_1 distortion as the primary order parameter is due to the trilinear coupling between U_1, L_2^-, and M_1^+ order parameters. This coupling leads to a simultaneous condensation of multiple order parameters at a temperature where all the second-order coefficients in the free energy expansion become positive [11, 74]. This is referred to as an 'avalanche-transition'. Since the avalanche transition is a first-order transition, it is impossible to the separate the primary and secondary order parameters as in an ordinary first-order phase transition. Hence, we refer to the order parameters only as 'primary-like' and 'secondary-like'.

[55] J. A. Holy, M. V. Klein, W. L. McMillan, and S. F. Meyer, Raman-active lattice vibrations of the commensurate superlattic in $2H - TaSe_2$, Phys. Rev. Lett. **37**, 1145 (1976).

[56] N. Nagaosa and E. Hanamura, Microscopic theory on the Raman spectra of transition metal dichalcogenides in CDW state, Solid State Commun. **41**, 809 (1982).

[57] Z. Wang, Charge density wave and possible Majorana zero modes in kagome superconductor CsV_3Sb_5, Workshop on "Correlated and topological states in Kagome metals", Quantum Foundry, UCSB (Oct. 18-21, 2021).

[58] In Eq. 7, m has the unit of the mass in analog of a two-dimensional harmonic oscillator.

[59] T. P. Devereaux and R. Hackl, Inelastic light scattering from correlated electrons, Rev. Mod. Phys. **79**, 175 (2007).

[60] M. V. Klein, Theory of raman scattering from charge-density-wave phonons, Phys. Rev. B **25**, 7192 (1982).

[61] N. Nagaosa and E. Hanamura, Microscopic theory on the raman spectra of transition metal dichalcogenides in cdw state, Solid State Communications **41**, 809 (1982).

[62] M. Kang, S. Fang, J.-K. Kim, B. R. Ortiz, J. Yoo, B.-G. Park, S. D. Wilson, J.-H. Park, and R. Comin, Twofold van Hove singularity and origin of charge order in topological Kagome superconductor CsV_3Sb_5 , arXiv:2104.05556 (2021).

[63] Z. Wang, S. Ma, Y. Zhang, H. Yang, Z. Zhao, Y. Ou, Y. Zhu, S. Ni, Z. Lu, H. Chen, K. Jiang, L. Yu, Y. Zhang, X. Dong, J. Hu, H.-J. Gao, and Z. Zhao, Distinctive momentum dependent charge-density-wave gap observed in CsV_3Sb_5 superconductor with topological Kagome lattice , arXiv:2104.05556 (2021).

[64] Q. Yin, Z. Tu, C. Gong, Y. Fu, S. Yan, and H. Lei, Superconductivity and normal-state properties of Kagome metal RbV_3Sb_5 single crystals, Chin. Phys. Lett. **38**, 037403 (2021).

[65] D. Wulferding, S. Lee, Y. Choi, Q. Yin, Z. Tu, C. Gong, H. Lei, and K.-Y. Choi, Fermi surface instabilities in electronic Raman scattering of the metallic kagome lattice CsV_3Sb_5, arXiv:2108.11690 (2021).

[66] M. Ye, E. W. Rosenberg, I. R. Fisher, and G. Blumberg, Lattice dynamics, crystal-field excitations, and quadrupolar fluctuations of $YbRu_2Ge_2$, Phys. Rev. B **99**, 235104 (2019).

[67] H. Miao, H. X. Li, W. R. Meier, A. Huon, H. N. Lee, A. Said, H. C. Lei, B. R. Ortiz, S. D. Wilson, J. X. Yin,

M. Z. Hasan, Z. Wang, H. Tan, and B. Yan, Geometry of the charge density wave in the kagome metal AV$_3$Sb$_5$, Phys. Rev. B **104**, 195132 (2021).

[68] T. Qian, M. H. Christensen, C. Hu, A. Saha, B. M. Andersen, R. M. Fernandes, T. Birol, and N. Ni, Revealing the competition between charge density wave and superconductivity in CsV$_3$Sb$_5$ through uniaxial strain, Phys. Rev. B **104**, 144506 (2021).

[69] W. Hayes and R. Loudon, Scattering of light by crystals (Dover Publications, Inc, 1978).

[70] Whether six-fold rotational symmetry is preserved or not depends on the system.

[71] E. Kroumova, M. I. Aroyo, J. M. Perez-Mato, A. Kirov, C. Capillas, S. Ivantchev, and H. Wondratschek, Bilbao crystallographic server: Useful databases and tools for phase-transition studies, Phase Transit. **76**, 155 (2003).

[72] P. G. Klemens, Anharmonic decay of optical phonons, Phys. Rev. **148**, 845 (1966).

[73] J. Menéndez and M. Cardona, Temperature dependence of the first-order raman scattering by phonons in si, ge, and $\alpha - $ Sn: Anharmonic effects, Phys. Rev. B **29**, 2051 (1984).

[74] I. Etxebarria, J. M. Perez-Mato, and P. Boullay, The role of trilinear couplings in the phase transitions of aurivillius compounds, Ferroelectrics **401**, 17 (2010).